Master's Theses (2009 -)   Dissertations, Theses, and Professional Projects

Effect of Low Reactivity Fuel on Reaction Wave Growth of Dual-Fuel Stratified Mixtures in a Rapid Compression Machine

David J. Roulo
Marquette University

EFFECT OF LOW REACTIVITY FUEL ON REACTION WAVE GROWTH OF DUAL-FUEL STRATIFIED MIXTURES IN A RAPID COMPRESSION MACHINE

by

David Roulo

Milwaukee, Wisconsin

August 2019

ABSTRACT
EFFECT OF LOW REACTIVITY FUEL ON REACTION WAVE GROWTH OF
DUAL-FUEL STRATIFIED MIXTURES IN A RAPID COMPRESSION MACHINE
David Roulo
Marquette University, 2019

For over 40 years, researchers have been studying homogenous charge compression ignition (HCCI) as a combustion strategy to improve the efficiency and emissions of the internal combustion strategy. Although early results were promising, it has been since discovered that HCCI engines only operate to their potential over a narrow load band. To remedy this, introducing inhomogeneities has been suggested as a method of controlling HCCI combustion in such a way to improve its usefulness. One such inhomogeneity is referred to as fuel octane number stratification and consists of port injecting a low reactivity fuel, allowing it to become well mixed, and then direct injecting a high reactivity fuel to introduce local mixture stratifications. Reciprocating engine and computational studies have shown this to improve efficiency and emissions of compression ignition engines, however, there has been little work done to explore octane number stratification on a per stroke basis in well-controlled conditions.

The objective of this study is to utilize fuel octane number stratification combustion strategy to optically observe the influence of the low-reactivity fuel, propane, on the dynamics of the reaction zone growth. To accomplish this, a rapid compression machine (RCM) was used to perform experiments in which combustion was captured by a high-speed camera. The RCM was outfitted with heaters and a polycarbonate window to control the temperature and optically access the cylinder. In addition, the mixture composition of propane to n-heptane was varied while keeping the global equivalence ratio constant at three unique initial temperatures.

The results of this study showed that ignition time, reaction front start location, and reaction front speed was sensitive to the amount of propane in the mixture. As propane content was decreased the time for the mixture to ignite relative to the start of compression decreased. Furthermore, as propane content decreased, the origin of the reaction front(s) increased in height along the cylinder wall. Reaction front velocity also increased as propane content decreased. Finally, through this work it was also discovered that ignition time and the reaction front speed of some mixtures were sensitive to changes in initial and compressed temperature.

ACKNOWLEDGEMENTS

TABLE OF CONTENTS

LIST OF TABLES

1.   Introduction

1.1   Motivation

Over 40 years ago, Onishi et al. [1] and Noguchi et al. [2] studied strategies to reduce exhaust pollutants and decrease fuel consumption in two-stroke engines. Onishi et al. studied the lean combustion of two stroke, spark-ignition (SI) engines for over ten years and found a way to control the irregular combustion and autoignition which were weak points of that engine [1]. They dubbed the method "Active Thermo-Atmosphere Combustion" (ATAC) and concluded that while ATAC was different from conventional combustion processes of engines of the time and required a shift from SI to compression ignition (CI), ATAC was easily adaptable to two-stroke SI engines and ATAC systems made possible immense improvements in fuel consumption and exhaust emissions [1]. In studying the instability and high fuel consumption of two-stroke engines at light-load conditions, Noguchi et al. encountered self-igniting combustion and found that to be very stable with low hydrocarbon emissions and improved fuel consumption [2]. In addition, they found that self-ignited combustion occurred at relatively low cylinder temperature [2]. These ideas eventually became known as the beginning of the homogenous charge compression ignition (HCCI) engine strategy. In HCCI engines, physical processes, like spark plugs or glow plugs, are not relied upon to control combustion. Instead, the cylinder charge consists of a homogenous mixture of fuel, air and exhaust products [3]. The engine behaves like a compression ignition engine, but chemical kinetics of the reacting fuel/air mixture are controlled by temperature and species concentrations [3]. Furthermore, this combustion is not characterized by knock, but by a smooth energy

release that does not damage the mechanical components of the engine [3]. A few years later and building on the work of Onishi et al. and Noguchi et al., Najt and Foster studied the mechanisms that govern HCCI combustion and how the process is altered by various engine parameters [3].

Ultimately Najt and Foster, along with others [3]–[6], found that HCCI engines present an attractive solution to the major issues plaguing commercial diesel compression ignition CI engines by being able to operate at high efficiencies due to less throttling required for part-load operation, leading to smaller pumping losses. Furthermore, combustion occurs at low temperatures, leading to low NOx emissions and in addition soot emissions are reduced [3]–[6]. Unfortunately, HCCI strategies only appear to be practical on a narrow band of low operating loads mainly due to difficulties controlling the heat release rate and combustion phasing at higher loads [6]. Mixture inhomogeneities has become a primary strategy to address HCCI's difficulties pertaining to heat release rate and combustion phasing. Many studies explored the effects of temperature inhomogeneities, or thermal stratification, and it's potential to control the heat release rates in HCCI engine strategies [7]–[9]. Dec et al. concluded that mainly thermal stratification within the bulk gasses controls the maximum pressure rise rate (PRR) and that natural charge stratification significantly reduces the maximum PRR, allowing higher loads than a homogenous charge [7]. Sjöberg and Dec also found that thermal stratification was a potentially viable option for extedning the upper load limits of HCCI engines and they performed experiments and ran multi-zone models that showed that enhanced thermal stratification can allow higher loads to be reached. In addition they coupled thermal stratification with combustion retard and found that as a viable

combination of strategy for controlling PRR [8]. In addition, Herold et al. found that a purely thermal stratification strategy produced a strong hot-to-cold progression in HCCI combustion, but also found that fuel concentration stratification reduced the effects of thermal stratification. However, Herold et al. concluded that it was unlikely that thermal or compositional stratification could control the PRR or control combustion because the stratifications showed that integral engine characteristics were only minorly effected when stratified flow fields were introduced into an HCCI engine [9].

To investigate thermal stratification on a fundamental level, some have sought to study HCCI combustion strategies using rapid compression machines (RCM) and have offered different strategies to try and control the rate of heat release and combustion phasing. The RCM was shown to be an excellent tool for these studies because of the simplifications of the mechanical system allowing for premixed charges without having to compete with residual gasses that a reciprocating engine would present, thus making it a good diagnostic tool [10]–[12]. Lim et al. studied thermal stratification as a solution to the issues with HCCI combustion using an RCM. Lim et al. found that thermal stratification leads to a lower rate of pressure rise and lower in-cylinder gas temperature than the homogeneous condition [10]. Nakano et al. also used an RCM to gain fundamental knowledge of the effects of thermal stratification on HCCI combustion and found that thermal stratification reduced the maximum rate of pressure rise across a variety of fuels and that thermal stratification prolonged the combustion process [11]. In addition, Strozzi et al. stated that RCMs are very well suited for HCCI combustion investigation and used an RCM to experimentally find the propagation regimes during autoignition with thermal stratification. Strozzi et al. also observed that in instances

where deflagration dominated the burning process, there was the lowest amount of heat release [12].

1.2 RCCI Background

Inagaki et al. investigated another method of HCCI engine control by using dual-fuel pre-mixed compression ignition (PCI) operation to reduce the necessity of EGR on PCI engine strategies, and in addition found that stratification of fuel reactivity resulted in reduced rates of heat release [13]. Sjöberg and Dec investigated the potential of partial fuel stratification to extend the upper load limit of HCCI combustion strategies and found that partial fuel stratification has the potential to increase the high-load limits for HCCI strategies [14]. In addition, they found that the two-stage ignition process allows more combustion retard compared to single-stage fuels [14].

The results of Inagaki et al. [13] demonstrated that blends of a low reactivity fuel (LRF) and a high reactivity fuel (HRF) are an effective strategy for advanced combustion strategy control. This basic combustion strategy has received significant attention and is now referred to as "reactivity-controlled compression ignition" (RCCI) combustion. Since then, numerous studies have been done regarding RCCI strategies [15]–[22]. Kokjohn et al. showed that fuel blending, causing fuel stratification, can be used to achieve acceptable NOx and soot levels, acceptable pressure rises [15], and ~50% thermal efficiency in a heavy-duty engine [23]. In addition, modeling showed that the duel fuel strategy led to staged combustion with the HRF igniting before the LRF [23]. Further experiments using the dual fuel strategy were reported by Kokjohn et al. [15] and

Hanson et al. [19]. They demonstrated in light-duty and heavy-duty engines that RCCI combustion can achieve gross indicated efficiencies over 50% for many operating conditions in addition to meeting the necessary NOx and soot limits without the use of expensive aftertreatments commonly found on diesel vehicles. In an optical investigation of RCCI combustion, [15] Splitter et al. suggests that RCCI combustion proceeds at different rates in different locations in the cylinder [16]. Kokjohn et al. for RCCI engines [24], [25], and Dec et al. for HCCI engines [4], [26] both rationalized the combustion phasing observed according the reactivity gradient introduced by the octane number and equivalence ratio stratification. They could not, however, quantify the actual speed of the reaction zone growth (RZG) wave with respect to a reactivity gradient.

1.3   Reaction Zone Growth Mechanism

Zeldovich laid the foundation of studying RZG when he identified five unique regimes of reaction front propagation: thermal explosion, supersonic auto-ignitive deflagration, developing detonation, subsonic auto-ignitive deflagration, and a conventional flame. [27]. When non-uniformities in initial temperature distributions or active radicals occur, there must be spatial distributions of autoignition delay times, therefore ignitions occur at various times in various positions. If front propagation is one-dimensional, and the autoignition delay time is a function of radius, $\tau(r)$ occurring at a radius, r, then the front propagates at a velocity, u_a, which is inversely proportional to the autoignition delay time gradient [27]:

$$u_a = \left(\frac{\delta \tau_i}{\delta r}\right)^{-1} \qquad\qquad (1)$$

However, if the front speed equals the local speed of sound, *a,* then the temperature gradient is at a critical value[27]. Gu et al. defined the dimensionless quality $\xi = a/u_a$ and defined the regimes found by Zeldovich in relation to ξ [28]. Gu et al. further stated that chemical resonance occurs at $\xi = 1$, [28] which corresponds to Zeldvich's definition for a "developing detonation" wave, which in an engine manifests as knock. Another dimensionless parameter, ε, characterizes the rate of chemical energy release, which is also hypothesized to affect the occurrence of developing detonation. ε is related to hot spot radius, r_o, the acoustic wave residence time, τ_a, and the excitation time, τ_e, as seen in Equation 2 [28], [29]:

$$\varepsilon = \frac{r_o/a}{\tau_e} = \frac{\tau_a}{\tau_e} \qquad\qquad (2)$$

Bates et al. used the plotted values of ξ against ε to define the peninsula within which detonations can develop from hot spot autoignition regimes, and defined the extent of the other autoignition regimes [30]. Bates et al. showed that the ξ and ε coordinates of the detonation peninsula are applicable over a wide range of fuels. In addition the ξ / ε plots can show the appropriate boundary at which auto-ignitive burning becomes less probable than deflagrative flame propagation and can identify the regimes of knock and super knock shown by Figure 1 [30]. These theoretical developments have relevance to HCCI improvement strategies, and the research utilizing these developments have primarily

focused on the abnormalities of combustion, *i.e.* knock, super-knock, low speed pre-ignition. The theory has not accounted for local equivalence ratio stratification or fuel octane number stratification, both of which would influence the reactivity gradient in a stratified combustion strategy.
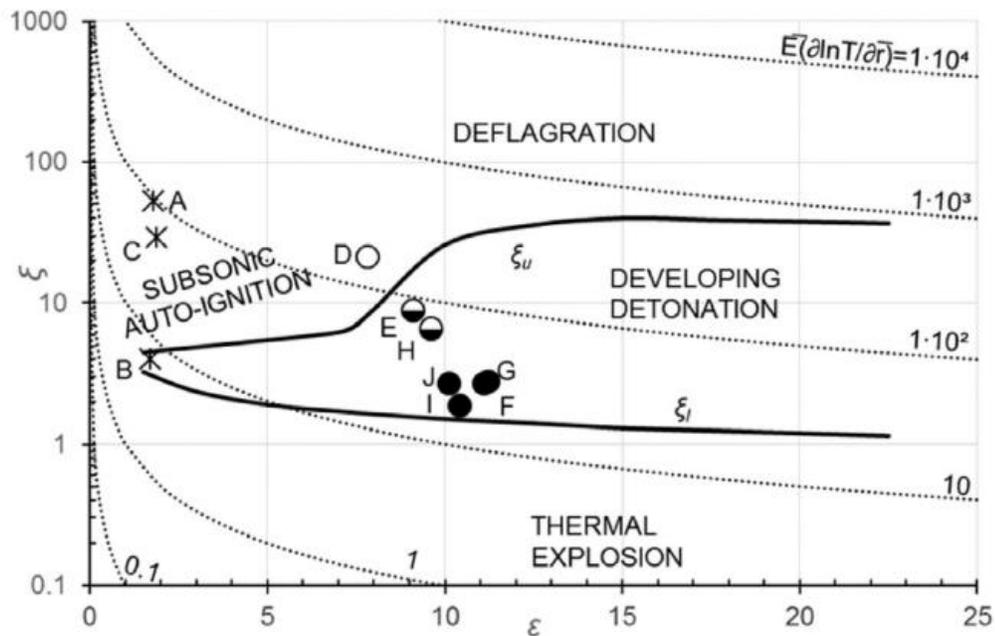
Figure 1: ξ/ε Plot Showing the Different Reaction Front Propagation Regimes. Increasing the black fill indicates the severity of knock at that condition [30].

Kokjohn et al. [24] recently studied to find the dominant mixing and ignition processes controlling RCCI combustion. By observing ignition locations and key features of the RZG, evaluating dependence of RZG on fuel reactivity stratification, and by isolating the roles of equivalence ratio (φ), temperature, and fuel blend stratification, Kokjohn et al. found that primary reference fuel (PRF) number stratification was the dominant factor in controlling the ignition location and rate of RZG. Equivalence ratio

had a smaller, but significant influence, and temperature stratification was found to be negligible due to the negative temperature coefficient (NTC) behavior of the PRF mixture [24]. Luong et al. seems to confirm the findings of Kokjohn [24] by showing that octane number stratification is dominant in the NTC region, but at higher temperatures, temperature stratification becomes dominant [31]. In addition, Luong et al. found, in different works, that using direct dual fuel stratification creates a diffusion driven reactivity gradient [32], [33]. These studies were DNS simulations that could not fully model the multi-scale effects in a three-dimensional environment. Actual experimental observations of in-cylinder behavior are needed to further advance the understanding of fuel reactivity stratification and how it can be used to control the heat release rates.

1.4   Rapid Compression Machine

A rapid compression machine (RCM) excels as a tool for studying high pressure combustion on a fundamental level. RCMs simulate a single compression stroke of an internal combustion engine and can have varying compression ratios, initial pressures, mixture temperatures, and mixture compositions. Compression occurs in less than 50 ms and peak pressures can easily exceed 50 bar along with temperatures greater than 1000 K. Generally, RCMs are used to study the autoignition of combustible mixtures, with a large focus on measuring ignition delay, of which an RCM can provide a direct measurement [34]–[41]. In addition, RCMs have been used to study reaction intermediates of different fuels in the negative temperature coefficient (NTC) regime and also, while RCMs are primarily set up for compression ignition, some RCMs have the capability to have spark

plugs fitted and can be used to study spark ignition [37], [42]–[44]. The ability to control many different variables of autoignition make the RCM and excellent tool of HCCI studies, where the goal is to control autoignition, especially when many retro fitted SI engines experience heavy physical damage from knocking that results from HCCI conditions [35], [45].

One drawback to RCMs is that different RCMs under different conditions can supply different results to experiments. These differences arise due to complicated aerodynamic and heat loss effects in the different RCMs [35], [37], [46]. In addition, temperature is a calculated value in RCMs, not a measured one, because of the rapidness of the compression and ignition process that occurs in less than 100 ms. The pressure trace used to indirectly determine temperature using a technique known as the "adiabatic core hypothesis" [35], [46]. This assumption only holds if heat loss is limited to the boundary layer, but if it breaks down, there is difficulty in obtaining a reasonable estimation for combustion temperature. Lastly, many studies have included optical access to the combustion chamber of a RCM, including side wall optical access and the utilization of Bow-ditch style pistons[47]–[50]. The ease of optical access in conjunction with the ability to control many parameters of combustion make the RCM an excellent tool to study fundamental nature of RCCI combustion.

1.5   Objective

Among the stratification strategies used, thermal stratification has been well characterized from fundamental studies using RCMs, to actual engine studies, and

modeling. However, fuel stratification strategies have primarily been studied in actual engines and in modeling, but there has been little work in a well-controlled reactor like an RCM. In addition, the vast majority of octane number stratification studies work within the range of fuel RON numbers from diesel to gasoline. The present study will utilize a RCM and a dual-fuel stratification strategy utilizing a simple diesel surrogate *n*-heptane, the high reactivity fuel (HRF), with propane, the low reactivity fuel (LRF). The objective of this study is to utilize fuel octane number stratification combustion strategy to optically observe the influence of the low-reactivity fuel, propane, on the dynamics of the reaction zone growth.

1.6   Structure of Thesis

This thesis is divided into four sections, each with a number of sub-sections. The following is a brief overview of each section.

Section 2 details the tools and methods for completing the experiments. The section begins with an overview of the RCM, followed by the method in which the RCM is heated. Next, the means of making the RCM optically accessible are discussed, followed by the method for image capturing. Section 2 continues with an extensive discussion of the fuels and the method in which they are injected, including a discussion on the usage of the GC-MS for verifying the fuel mixing strategy. The section ends with a brief summary of the experimental procedure and the key variables.

Section 3 contains the results and the subsequent discussion of the results. This section begins by presenting qualitative findings from pressure plots and image data. Next, section 3 discusses how the qualitative findings were extracted from the images and pressure data, and finally these findings are discussed in detail.

Section 4 is the conclusion and future improvements section. This section provides a summary of the main conclusions developed in section 3. In addition, this section ends with a discussion on how these experiments could be improved and what future work might exist as a relevant follow-up to this thesis.

2. Experimental Methods

This section details the equipment and method used to perform the experiments. It begins with an overview of the RCM, followed by a description of the modifications made to the RCM for the purpose of these experiments, including creating the heating system, creating the optical accessibility, and the addition of a second fuel injector. Next, the chosen fuels, along with the injection and mixing strategies are discussed, including the description of GC-MS testing that proved the mixing of the propane and air to be "well-mixed." Finally, this section concludes with a summary of the experimental procedure and variables.

2.1   Rapid Compression Machine

The primary tool for this study is the Marquette University rapid compression

machine (RCM). Detailed specifications and design are stated by Neumann, however a brief overview of the design and functionality will follow [34]. The RCM is driven by a pneumatically actuated cam, as shown in Figure 2 and interchangeable into a rapid compression-controlled expansion Machine (RCCEM) by changing cams.
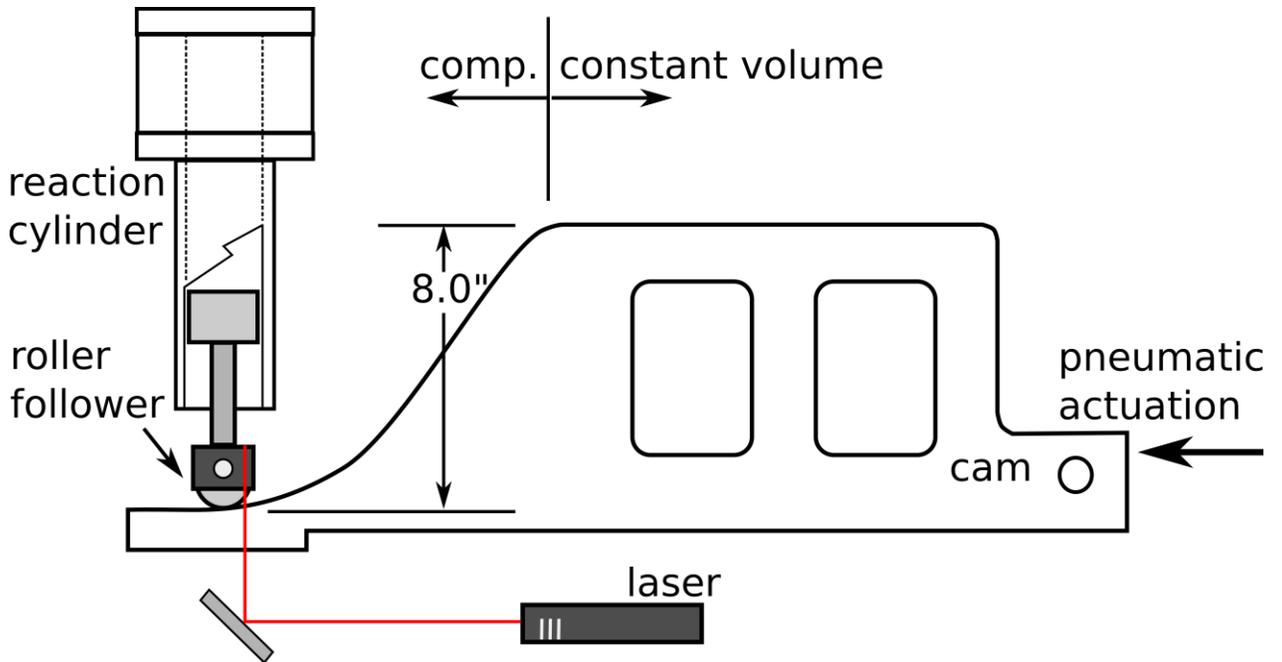
Figure 2: RCM Cam

For this study, only the RCM cam is used, thus constant volume is maintained after compression. In addition, to being pneumatically actuated the RCM is hydraulically stopped and operates using the rapid mechanical stroke of the piston to generate high pressures and temperatures to initiate combustion under a controlled volume. The RCM uses a creviced piston modeled after the design of Mittal and Sung [39]. Other design characteristics of the RCM are described in Table 1.

Table 1: RCM Operating Characteristics [34]

Cylinder Bore Diameter	2 in
Stroke Length	8 in
Compression Ratio	4-17
Clearance Height	0.5-1.5 in
Compression Time	~30-50 ms

The dynamics of the cam-style RCM are as follows: when the hydraulic stop is released, the pneumatically driven rod attached to the cam accelerates. At the base of the combustion piston rod there is a roller that sits on the cam, and as the cam moves, the piston roller follows the profile of the cam to compress the gas mixture.

2.2   *Heating the RCM*

To properly evaluate the effect of the dual-fuel stratification, it was necessitated that the inner air temperature of the RCM is held to a constant, even temperature throughout the entirety of the stroke. To do this a heating system was developed. First, seven 500 W band heaters were placed at certain locations along the length of the stroke along with five Omega K-type thermocouples. The locations can be seen in the schematic shown in Figure 3.
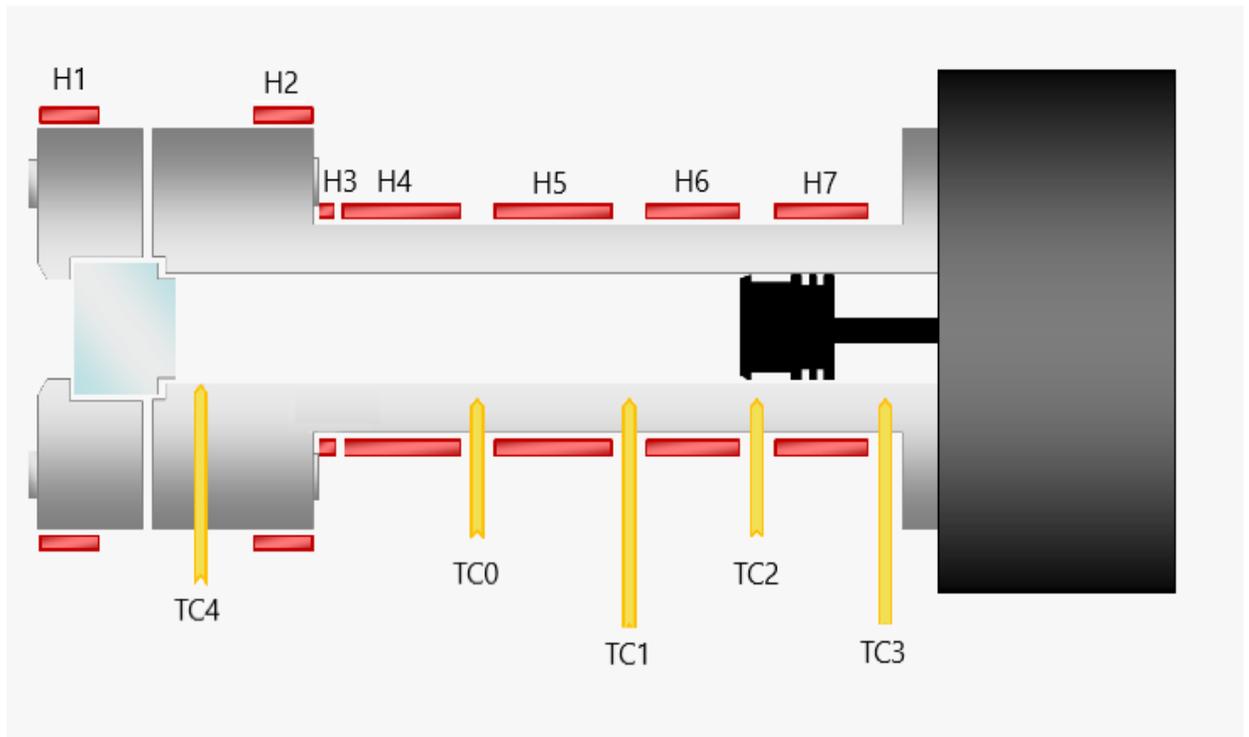
Figure 3: Heater and Thermocouple Locations

The band heaters are compatible with 120 V power and the end of the wires were soldered and inserted into plug-in receptacles so that the heaters could be easily disconnected on an individual basis for any necessary maintenance. The heaters were then plugged into a custom-built electrical box as seen in Figure 4. The box housed solid-state relays that were connected to the heaters and functioned as the switch to power on and off. The relays were powered from wall power through the terminals at the bottom of the electrical box. The relays are commanded on or off based on a custom LabVIEW VI, based on a similar VI developed by Dr. Casey Allen. The hardware that interfaces with the VI is a Measurement Computing USB-TC DAQ that inputs the thermocouple signal and outputs a digital signal to the VI to command the relays on or off to turn the heaters

on or off. The heaters are specifically controlled by a PID controller, developed solely by

Allen, within the VI. Each of the seven band heaters is governed by a user defined

setpoint and takes in data from either one or an average of thermocouples to decide what

temperature its location is currently at and how much power is required to increase it, if

that is deemed necessary.
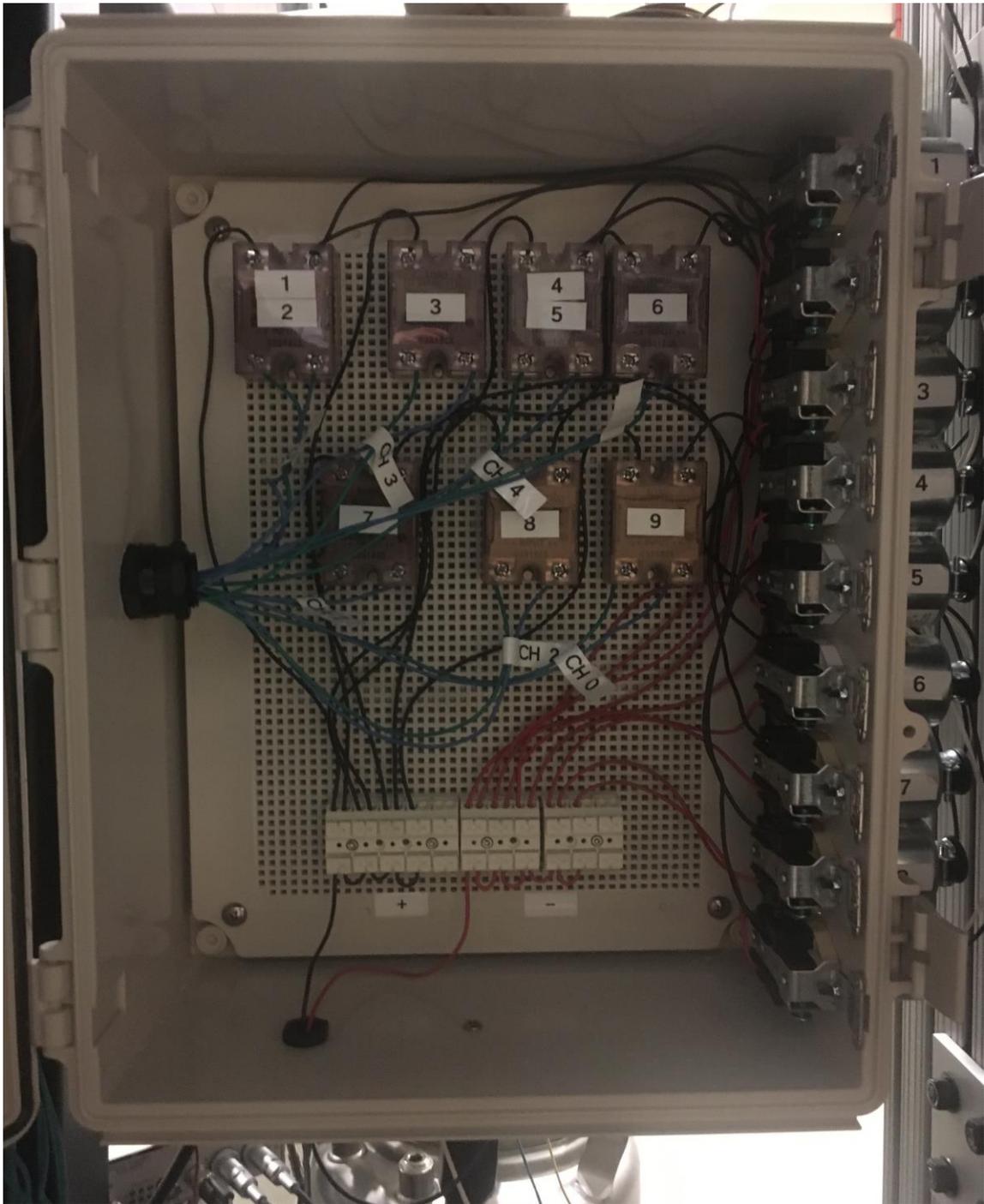
Figure 4: Heater Electrical Box

Table 3 shows the heaters and the thermocouples their on/off state is dependent on, using the identifications from Figure 3.

Table 2: Heater/Thermocouple Dependency Information

Heater ID	Dependent Thermocouples
H1	TC4
H2	Average (TC4, TC0)
H3	Average (TC4, TC0)
H4	Average (TC4, TC0)
H5	Average (TC0, TC1)
H6	Average (TC1, TC2)
H7	TC3

Since H7 is behind the piston, its main job is to minimize the temperature gradient, to minimize heat loss, out of the back of the cylinder. The mixture is unaffected by the lower H7 temperature, and if H7 was forced to meet the same temperature of the other heaters, it ends up driving H6 up too high. It is assumed that there is no stratification due to the lower H7 temperature because H7 is behind the piston and the mixture cannot diffuse behind the piston due to the piston rings, thus H6 is assumed to be the last heater location the mixture can interact with. Lastly, the efficiency of the heaters and constant uniformity is greatly improved by wrapping the RCM in 1" thick mineral

wool insulation. The thermal conductivity of the mineral wool is 0.23 W/m °C according to the supplier, McMaster-Carr [51]. Given that thermal conductivity, using the 1-Dimensional conduction equation [52], it was determined that at the highest tested temperature, the determined rate of heat loss is 1.5 W, which is minimal. The low rate of heat loss coupled with the consistency of the temperature uniformity determined that the 1" thick mineral wool was sufficient. Finally, to achieve the uniformity for the three temperatures tested at, seven setpoints for each uniform temperature is needed, Table 3 show the set point at each heater for each temperature.

Table 3: Heater Setpoints

Heater Number	Heater Setpoint at 303 K/313 K/323 K
H1	303 K/313 K/323 K
H2	303 K/311 K/321 K
H3	303 K/311 K/323 K
H4	303 K/313 K/320 K
H5	303 K/312 K/322 K
H6	303 K/313 K/323 K
H7	296 K/298 K/299.6 K

2.3   Optical Set-Up

The combustion chamber of the RCM is optically accessible from the front view. The window into the combustion chamber is a 0.5" thick clear and polished polycarbonate disk with a 2.3" diameter, with 2" of the diameter providing an unobstructed view to the through the cylinder. Figure 5 shows a section view of the front flange of the RCM where the window is housed.
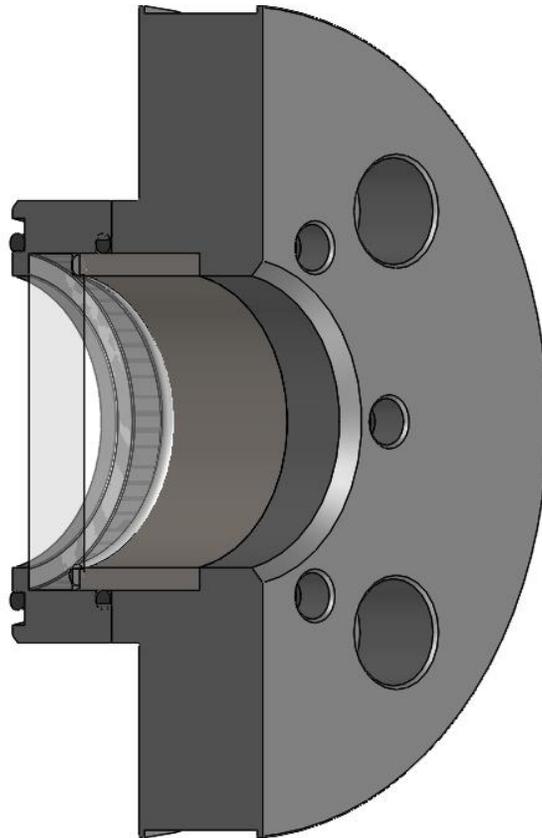
Figure 5: RCM Head Window

The main reason for polycarbonate was chosen was because it was readily available and relatively inexpensive. However, according the source for the polycarbonate, Midland Plastics, the window transmits 88% of visible light [53] which is acceptable for this study. In addition, to make sure 0.5" thick polycarbonate disk would hold up safely under high pressures, a simple finite element analysis was run. Figure 6 and Figure 7 show the results of that simulation. For this simulation, the window was fixed in the x, y, and z directions on the backside, and a uniform pressure of 100 bar was applied to the front side. 100 bar was chosen because it was the highest pressure expected to see in the RCM.
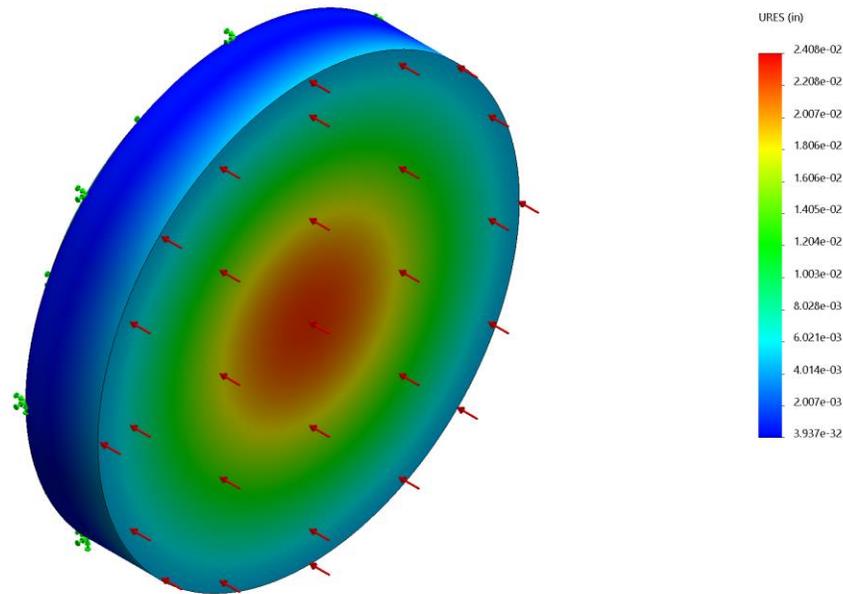
Figure 6: Deflection of RCM Window at 100 bar
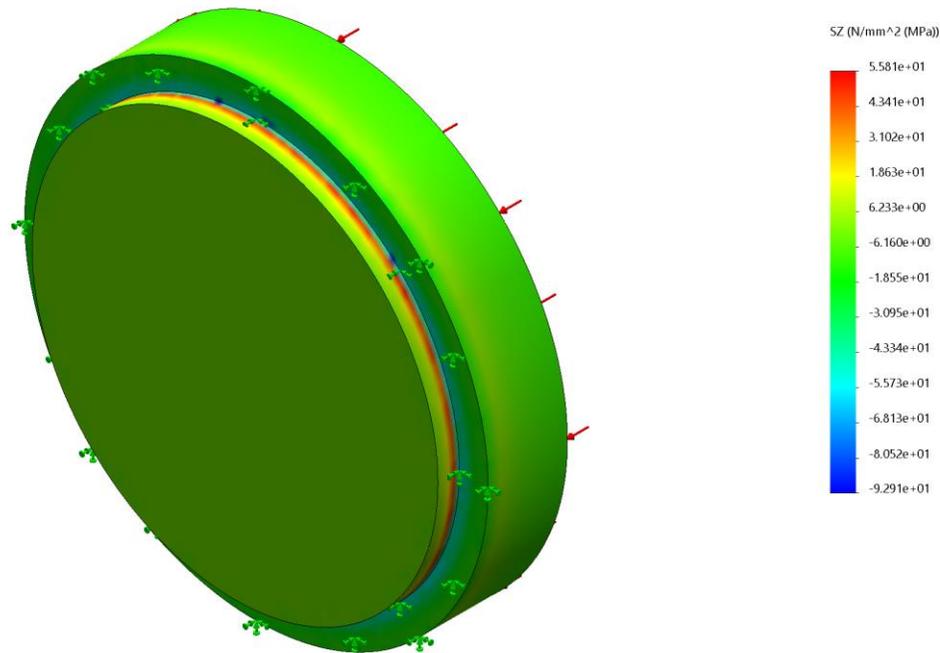
Figure 7: Normal Direction Stress on RCM Window at 100 Bar

At 100 bar it was observed that the window would deflect 4.8% of the thickness and the maximum stress would occur at the edge where the clamp holds it in place. That maximum stress is 55.81 MPa, which is well under the manufacturer's published flexural strength of 75.84 MPa [53]. However, this study does not indicate an infinite life for the window, and testing proved that a window was only good for approximately 50 RCM tests. At approximately 50 tests, surface cracks would appear on the window, which indicated a need for the window to be changed. Combustion is recorded by a Photron Fastcam APX RS with a1:2.8D Nikon AF Micro NIKKOR 105 mm. The camera records the images at 30,000 fps and is controlled by a LabVIEW VI trigger that triggers after a set pressure rise is seen by the VI.

2.4 Fuel Injection System of the RCM

2.4.1 Fuel Choice

RCCI combustion strategies focus on compression ignition engines, namely commercial diesel engines, light or heavy duty[15]–[22]. Thus, to increase the relevance of this study, diesel fuel, or more specifically, a laboratory grade diesel fuel surrogate is needed. *n*-Heptane has been identified as an important diesel surrogate [54] and >99% pure *n*-heptane is used in this study. Since *n*-heptane has a research octane number, or RON, of 0, it acts as the HRF [55]. The research octane number is a measure of the performance of a fuel, or its resistance to ignite. The higher the RON, to more compression the fuel requires to ignite. Therefore, the less resistance a fuel has towards ignition, the more reactive it is and vice-versa. For the LRF, gasoline, or its surrogate, *iso*-octane has been used [15], [19], [24] and primary reference fuel (PRF) number stratification has been observed. *iso*-Octane has a RON of 100 [55] which makes it a quality LRF, however this study sought to try and exaggerate the effects of the LRF to obtain more notable effects, so a higher RON number fuel was sought. Some RCCI studies have used propane as the low reactivity fuel in diesel studies and have found that the addition of propane helped to reduce particulate matter (PM) and significantly reduces the combustion temperature resulting in lower NOx emissions [56]–[58]. In addition, propane is a highly volatile fuel and is in a gaseous state at standard pressure and temperature, and this makes propane useful for premixing with air. Furthermore, the RON of propane is between 109.4 to 112.5 [59], [60] thus giving it a higher RON than

iso-octane. In addition, propane is a common fuel to purchase, therefore instrument grade propane was chosen as the LRF for this study.

2.4.2 Fuel Injection

The fuels are injected into the chamber using two direct injectors (Bosch 0261), modeled after the "direct test chamber" method described by Allen et al. [61]. Injection is controlled by the Cal-View injection software. *n*-Heptane is fed from an accumulator pressurized at 800 psi and propane is fed directly from the pressurized tank at 48 psi. Prior to testing both injectors are calibrated. The calibration process consists of setting the RCM chamber to a pressure between 0.100 bar and 0.200 bar and injecting fuel. The pressure increase is then measured after the fuel is injected and the ideal gas law allows for the conversion of pressure increase to mass of fuel injected. The mass injected is then recorded over a range of injector pulse widths, and ideally the relationship between mass injected and pulse width is linear. If the relationship is not linear than that injector is not used. Figure 8 shows the linear curve for the *n*-heptane injector and Figure 9 shows the linear curve for the propane injector.
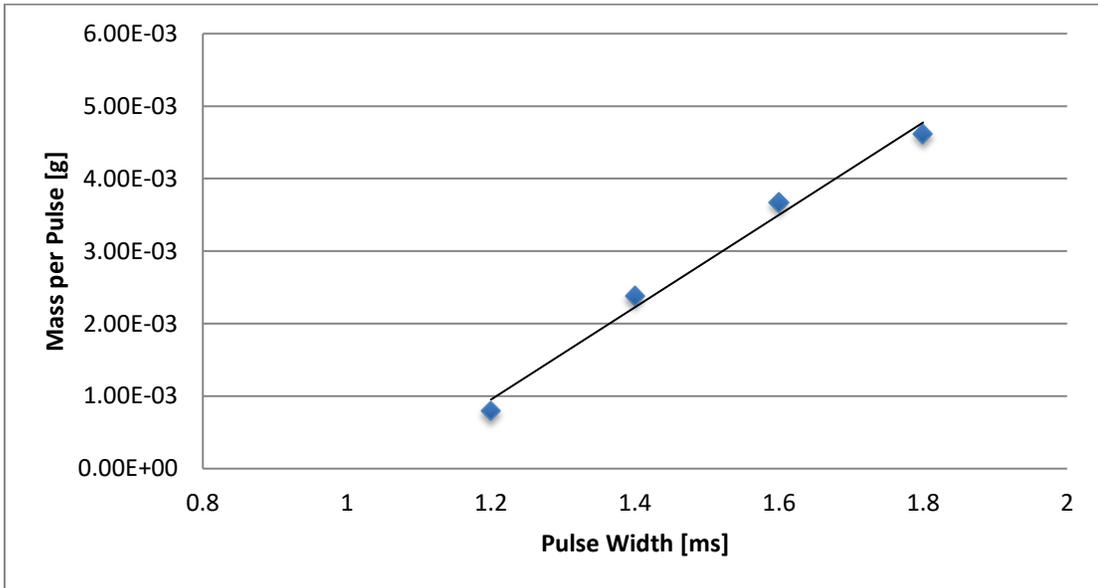
Figure 8: *n*-Heptane Injector Curve

The R^2-vale for the *n*-heptane injector is 0.9874 therefore its linearity is confirmed.
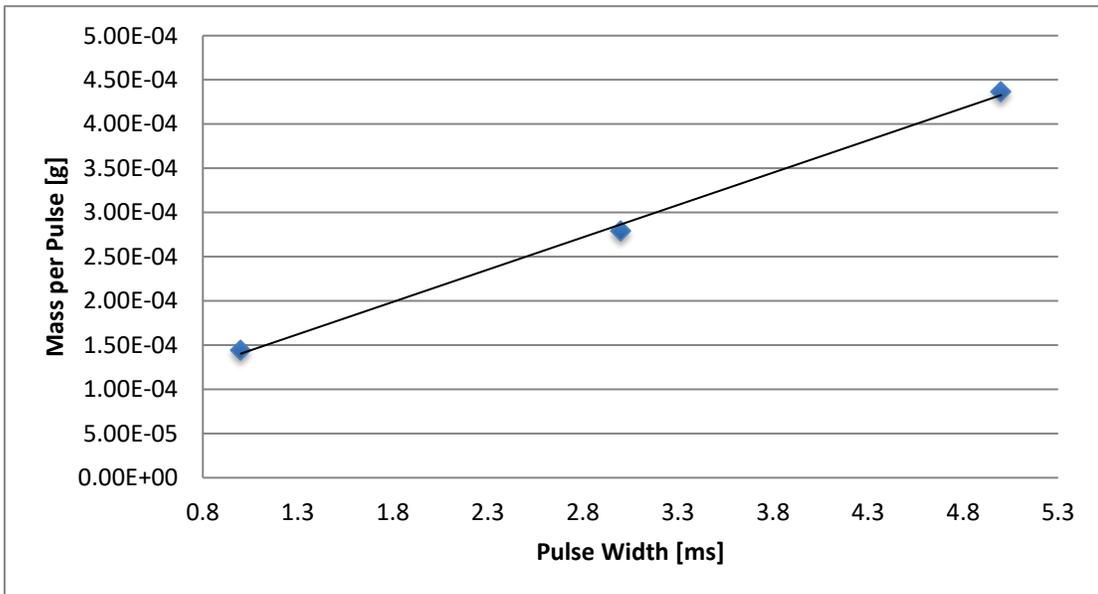
Figure 9: Propane Injector Curve

The R^2-value for the propane injector is 0.9981, therefore the linearity is also confirmed. Furthermore Equation 3 and Equation 4 show the linear equation for the injectors that is used to predict the mass injected based on the pulse width (PW).

$$m_{C_7} = 0.0064PW - 0.0067 \qquad (3)$$

$$m_{C_3} = 7 \times 10^{-5}PW + 7 \times 10^{-5} \qquad (4)$$

For this study, the equivalence ratio for the fuel mixture is held constant at 0.6, however, the mole fraction, X, was varied for the various tests. The equivalence ratio of 0.6 was chosen because it upon review of an RCCI review paper [22] 0.6 was a median equivalence ratio that was being tested in literature. Table 4 shows the various mole fractions of the fuels that were injected at $\varphi = 0.6$.

Table 4: Fuel Mole Fraction

X_{C3}	X_{C7}
0.9	0.1
0.8	0.2
0.7	0.3
0.6	0.4
0.5	0.5

To find the mass needed to inject to satisfy the criteria in Table 4, a form of the ideal gas law was utilized, shown by Equation 5.

$$n_f = \frac{V_0 P_0 X_{O_2} \varphi}{R_u T a_s} \tag{5}$$

Where n_f is the total number of moles for the mixture, P_o is initial pressure [Pa], R_u is the universal gas constant [J/mol*K], and T is temperature [K]. V_o [m³] is the volume defined by Equation 6.

$$V_o = V_{Stroke} + V_{Clearance} + V_{Crevice} + V_{Dead} + V_{Offset} \tag{6}$$

Equation 7 defines a_s as it was used in Equation 5 [6].

$$a_s = X_{C_3H_8}\left[x_{C_3H_8} + \frac{y_{C_3H_8}}{4}\right] + (1 - X_{C_7H_{16}})\left[x_{C_7H_{16}} + \frac{y_{C_7H_{16}}}{4}\right] \tag{7}$$

Where X is mole fraction, x is number of carbon atoms, and y is number of hydrogen atoms. The necessary mass injected for of a fuel is then determined using Equation 8 and Equation 9, where MW is molecular weight [g/mol].

$$m_{C_3} = X_{C_3} MW_{C_3} n_f \tag{8}$$

$$m_{C_7} = X_{C_7} MW_{C_7} n_f \tag{9}$$

The results of Equation 8 and Equation 9 are then plugged into the linear equations, Equation 3 and Equation 4, and the pulse width is determined. Finally, the number of pulses is determined by the ratio of total fuel mass to be injected to mass per pulse. Table 5 shows the pulse width and number of pulses for each condition used.

Table 5: Fuel Injection Parameters

Condition	Pulse Width [ms]	Number of Pulses
0.9 Propane/0.1 n-Heptane	4.3570/1.2247	50/5
0.8 Propane/0.2 n-Heptane	3.5227/1.3039	50/5
0.7 Propane/0.3 n-Heptane	3.1369/1.3692	45/5
0.6 Propane/0.4 n-Heptane	2.7938/1.4238	40/5

2.5   Gas Chromatography

To verify the well-mixed assumption of the LRF for this study, an Agilent gas chromatograph is used with three different detectors: a mass spectrometer (MS), a flame ionization detector (FID), and a thermal conductivity detector (TCD). The FID and the MS are in line and the species are initially separated using a 3 m DB-1 Column and then further separated after flowing through a purged ultimate union by a 60 m Gas-Pro column before being sent through a non-purged ultimate union that sends the species at an equal amount and rate to the MS and FID. This allows for the easy identification of

most species because many of the species peaks will line up on the MS and FID spectrum. Furthermore, when sending species to the TCD, they first flowed through a Plot-Q column that provided initial species separation before they passed through the Dean Switch. The Dean Switch is a time dependent valve that is only open long enough to allow species with a molecular weight under 32 g/mol to pass. When the Dean Switch is open, the species are further separated by a Mol-Sieve Column and sent to the TCD, and when the Dean switch was closed, the species are vented.

In terms of usage for this study, the MS was used to identify the LRF, to verify that the LRF was the only component in the mixture besides air. The FID, the front detector, is used to quantify the concentration of all the fuels. This is done by taking the area under the FID peak corresponding with the fuel to be quantified, the units for this measurement are arbitrary and referred to as "area counts." Lastly, the back detector is the TCD which is used to detect non-combustible species of mass less than 32 g/mol, with its primary function being to quantify the air mixture. To capture the gasses in the RCM, the polycarbonate window is replaced with a plug containing a septum. A 0.5 mL Hamilton Sample Lock Syringe using a 2" non-coring needle is inserted through the septum into the RCM. The procedure for this follows the procedure described in the next section for loading the LRF in the RCM exactly, except the HRF is never injected and the RCM is never run. After the HRF is injected, the needle is inserted at the desired test time to a position along the stroke of the RCM and the syringe is filled to ensure consistency. The sample is then locked into the syringe and injected directly in the GC-MS bypassing the gas sampling loop to avoid sample dilution. Quantification of the LRF is completed using external standards. Since the LRF is injected as gaseous propane, a 2 L tedlar gas

sampling bag is filled with 100% propane. Then 0.5 mL of propane is extracted from the bag by the aforementioned syringe and injected into the GC-MS using the aforementioned procedure. Since the bag is filled with only propane, the area under the FID peak corresponding with propane corresponds with 1,000,000 ppm of propane, therefore a relationship between FID area counts and ppm is established.

After significant "trial and error" experimentation following the previously described methodology, the conditions for which the "well-mixed" assumption holds were discovered. First, after the propane is initially injected under a vacuum it is allowed to diffuse under a vacuum for 600s. The hypothesis was that this stage of mixing would promote the highest level of diffusion because the density gradients are greatest under a vacuum and the propane would be driven to diffuse until equilibrium. Following that 600s period, the desired mass of air is rushed in and then sealed in the combustion chamber. It was discovered that any period of time equal to or greater than 600s was sufficient to allow the air/propane mixture to settle into a well-mixed state. Evidence of this is shown by Figure 10, which shows the relationship between air/propane mixing time and propane concentration at the point of withdrawal by the syringe. It was assumed that if the propane concentration for multiple consecutive mixing times at the point of withdrawal was approximately equal to the theoretical concentration of propane that was calculated to be injected, then the mixture could reasonably be assumed to be well-mixed.
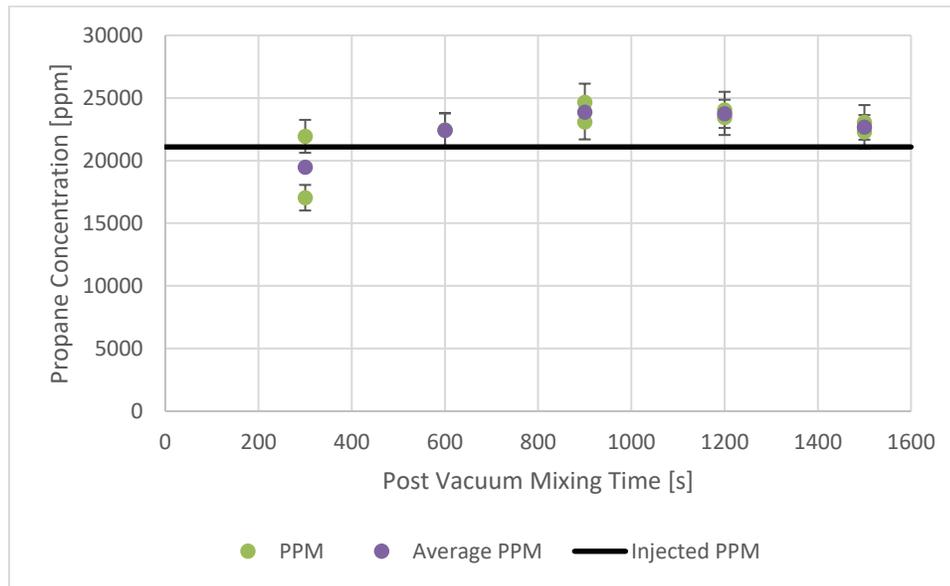
Figure 10: Well-Mixed Assumption Validation

The calculated theoretical value for injected concentration of propane was 21,096.4 ppm.
At and after 600s of air/propane mixing time, the error in measurements was within the 6%
error that is inherent to the GC-MS of the calculated value. Therefore, in the interest of
time, 600s of air/propane was chosen for all experiments.

2.6   Experimental Methodology and Variables

The following outlines the process for running a dynamic RCM RCCI
experiment. The LRF is injected first into the cylinder under a vacuum of 0.004 – 0.006
bar and left to diffuse under a vacuum for 600 seconds. After the 600s diffusing period, a
manifold separated from the cylinder from a poppet valve is then filled with synthetic air
and the poppet valve is opened allowing the air to rush in a mix with the injected
propane, and the pressure is monitored by a static pressure transducer (Omegadyne

PX409) whose output is recorded in LabView. The chamber is set to the desired initial

pressure and then the poppet valve is closed, sealing the combustion chamber. The

propane air mixture is allowed to mix for 600 seconds and at this point the mixture is

well mixed, as verified in Section 2.5.

After the LRF is injected and the time has passed such that the well-mixed

assumption is valid, the HRF is injected and the hydraulic stop is released after 5

seconds, which is a short enough time to ensure fuel reactivity stratification. The injectors

are controlled by the National Instruments Cal View program and during an experiment,

a piezoelectric pressure transducer (Kistler 6045A) measures the cylinder pressure and a

laser displacement sensor (Keyence IL-600) tracks the position of the combustion piston.

Finally, Table 6 summarizes all relevant test conditions for this study.

Table 6: Experimental Variables

LRF/HRF	Propane/n-Heptane
φ	0.6
HRF Fuel Mixture Fraction	0.1, 0.2, 0.3, 0.4
LRF Fuel Mixture Fraction	0.9, 0.8, 0.7, 0.6
Compression Ratio	10.06
T_0	313, 323, 333 K
P_0	1.060 bar
P_c	15 bar
LRF Vacuum Diffusion Time	600s
LRF Air Mixing Time	600s
HRF Evaporation Time	5 s

3. Results and Discussion

This section presents the results of the experiments in addition to a discussion of those results. Data for this section was gathered by the methodology discussed in section 2. With four different fuel mixes at three different temperatures, there were a total of twelve conditions tested. Each condition was tested three times, however upon analysis, there were six tests that were deemed outliers and unusable. Nine of the twelve cases are based on at least two tests. Three of the cases are only represented by one test, but that single test was deemed acceptable because when the data was viewed broadly, the general trends were preserved by those single test cases. To be considered an outlier a test had to have an issue with either the data acquisition that was not seen when the tests were running, or the metrics taken from the results were so far outside the standard deviation of the other tests at that case that a mistake in the mixture makeup had to have occurred and the test was thrown out. This section proceeds by first presenting basic qualitative findings that were made by simply examining the pressure plots and the image data. The quantitative findings are discussed and used in conjunction with methods found in literature to obtain relationships that were used to characterize and explain the results in terms consistent with the literature.

3.1 Observations from the Pressure Plots and Images

The standard combustion chamber pressure versus time data was collected for each experiment. This data Figure 11 shows the pressure versus time plots for the different

mixtures at each initial temperature. Figure 12 shows the pressure versus time plots for the different initial temperature, at each fuel mixture. Compression begins at approximately 80 ms, however, the camera was set to trigger when the pressure in the cylinder rose above 1.5 bar, which corresponds to a time of approximately 100 ms, which is why that was chosen as the starting point for the plots. For these experiments, piston top dead center (TDC) occurs at approximately 150 ms, corresponding with a compressed pressure of 15 bar. However, as is seen in Figure 11 and Figure 12 and will be seen in other later figures, often the mixture ignites before the piston reaches TDC. In addition, for the following figures, only one trace from each condition is shown, even though multiple tests were run, to present the data in a clear fashion.
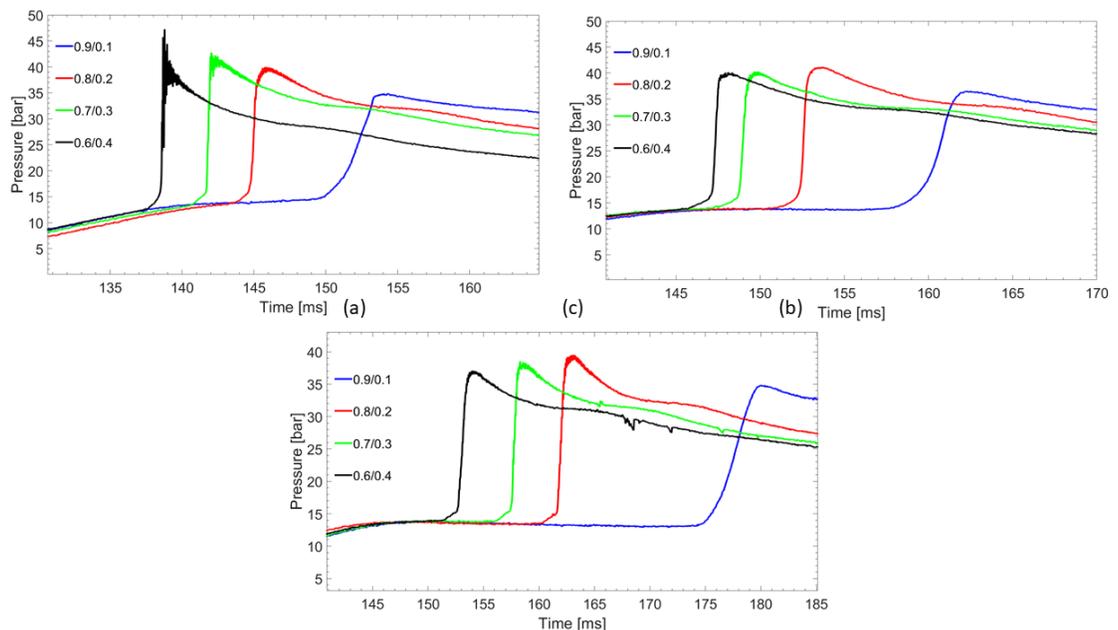
Figure 11: Pressure versus Time for each mixture at an initial temperature. (a): 323 K, (b): 313 K, (c): 303 K
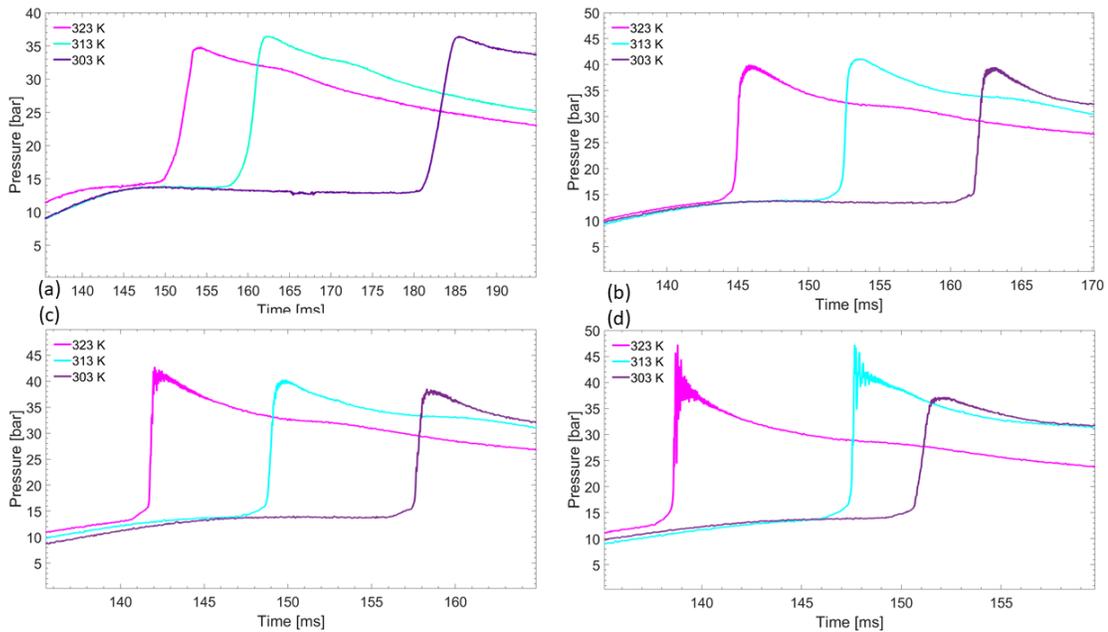
Figure 12: Pressure versus Time plot for mixture with differing initial temperatures. (a): 0.9/0.1 (b): 0.8/0.2

(c): 0.7/0.3 (d): 0.6/0.4

The largest observation from Figure 11 and Figure 12 is the effect the mixture composition and initial temperature have on when ignition begins. (Note: Normally, that time is referred to as "ignition delay time" however, ignition delay in RCM studies refers to the time between piston reaching TDC and the start of ignition. Since not every test has the piston reach TDC, the author does not want to misuse the term, and would like to preserve the definition of ignition delay for later in this section when it is referred to in the correct context. Therefore, the time in which ignition occurs will be referred to as "ignition time" or t_{ign} for this thesis in order to preserve the proper definition of ignition delay time.) The general trends are that as propane is increased, ignition time increases and as temperature decreases, ignition time increases. This is expected because propane, with a RON of about 109-112 is a low reactivity fuel which makes it more difficult to ignite, especially when

compared to *n*-heptane with a RON of 0. The expected role of propane in this study is to function as a retardant to the *n*-heptane. However, an interesting observation with regards to mixture composition is the gap in ignition time between the 0.9/0.1 case and the others. Regardless of temperature, the ignition time of the 0.9/0.1 cases are significantly longer, and even more interesting is the delta between the 0.9/0.1 case and the 0.8/0.2 case is longer, regardless of temperature, than the deltas of any of the other sequential cases. There were no unexpected observations with regards to initial temperature either. Since reaction rate is a function of temperature via the Arrhenius equation, a lower temperature would decrease the reaction rate, leading to a longer ignition time. However, Figure 12 also shows how the difference in ignition time is decreased as propane is decreased, especially when in regards from 0.9/0.1 to 0.8/0.2 and how similar the other three cases are to each other.

In addition to analyzing the pressure plots, the video images were also correlated to the pressure trace in time. Figure 13 shows the pressure versus time plot of the case with the longest ignition time, composition of 0.9/0.1 at 303 K, and Figure 14 displays a close up of the combustion event pressure trace annotated with high speed images. For all image

figures, the color was inverted to the darker areas denote the luminous emission from the

reaction.
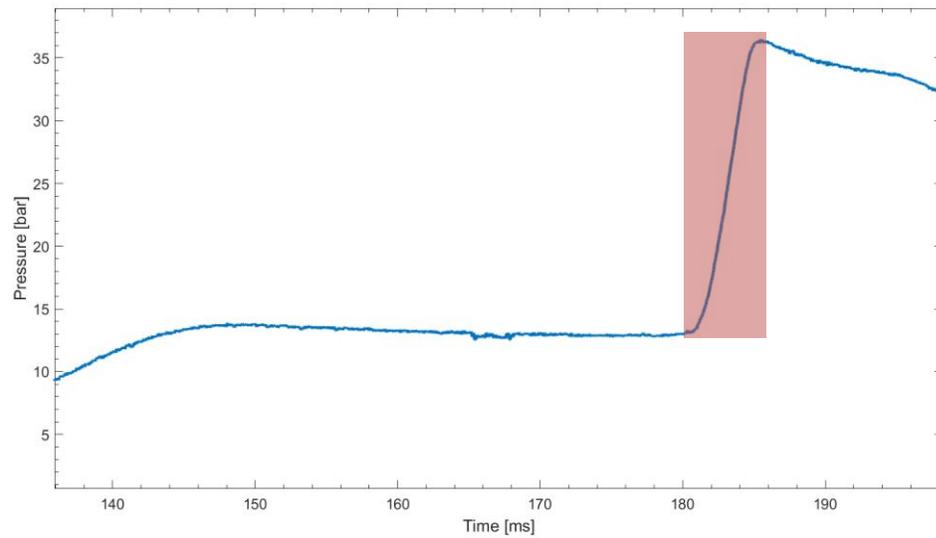
Figure 13: Pressure vs. Time Plot at 0.9/0.1 composition at 303 K which had the Longest Ignition Time.

Box shows the area chosen for the close-up
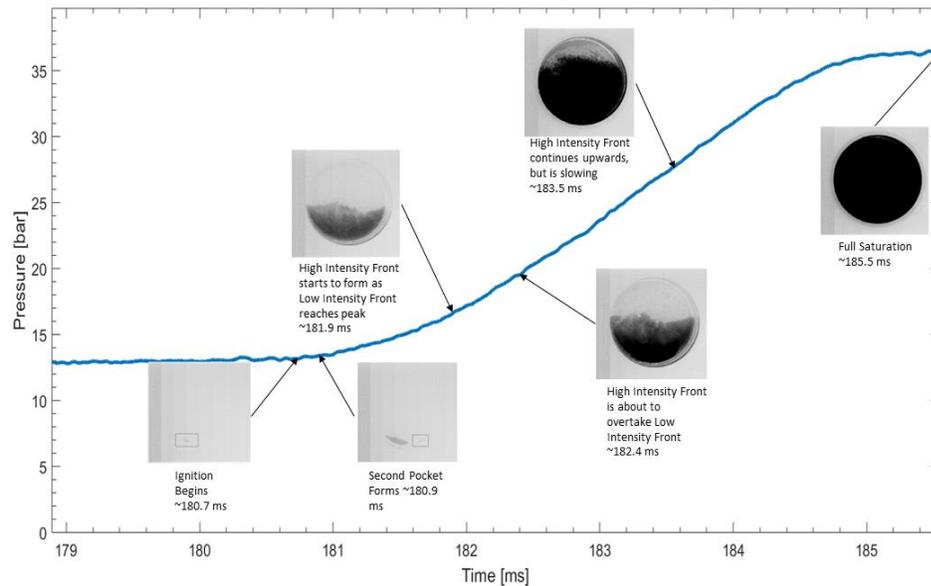
Figure 14: Close-up 0.9/0.1 Composition at 303 K Annotated with High Speed Combustion Images

When analyzing Figure 14, the first thing to note is the boxes in the first two images highlight the location of the start of ignition. Multiple ignition fronts form in many cases, and this case is no different with a second front forming approximately 60° from the first and only 0.2 ms later. Another phenomenon that was present in almost all cases was the presence of a low intensity front and the presence of a faster high intensity front. The low intensity front in the case of Figure 14 fills 50% of the cylinder 1.2 ms after the start of ignition, while the high intensity front overtakes the low intensity front and fills 50% of the cylinder after only 0.5 ms of forming. However, after overtaking the low intensity front the high intensity front takes double the time, 1.1 ms, to go from having 50% of the cylinder filled to 75% of the cylinder. Furthermore, to go from 75% filled to 100% filled or "full saturation" takes another 2 ms. To further elaborate on the relationship between the low intensity and high intensity fronts, Figure 15 shows the combustion event as it proceeds

after the two low intensity fronts combine up until the high intensity front completely overtakes the low intensity front.
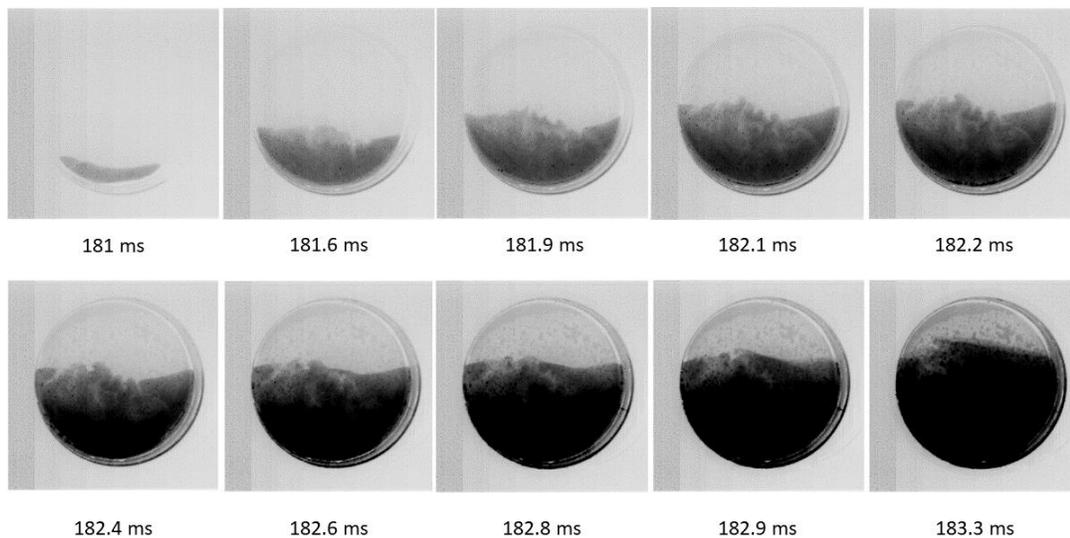
Figure 15: 0.9/0.1 Composition at 303 K Low and High Intensity Front Dynamics

The low intensity front expands quickly, covering about 50% of the cylinder, but then stalls out at that point. The stall point coincides with the formation of the high intensity front, and even though the low intensity front does seem to fill approximately 66% of the cylinder by the time the high intensity front overtakes it, it takes the same amount of time to move from 50% to 66% as it did to reach 50% after the front formation. One possible explanation for the stall is that the mixture becomes too lean because the fuel is being consumed by the low intensity front and, at the stall point, fuel is beginning to be consumed by the high intensity front as well, making the mixture even leaner. As the mixture becomes leaner, the reaction slows leading to the stalling of the low intensity front, and eventually to the dramatic slowing of the high intensity front.

Figure 16 looks at the most reactive case, the 0.6/0.4 case at 323 K, which yields the shortest ignition time and Figure 17 displays a close up of the combustion event pressure trace annotated with high speed images.
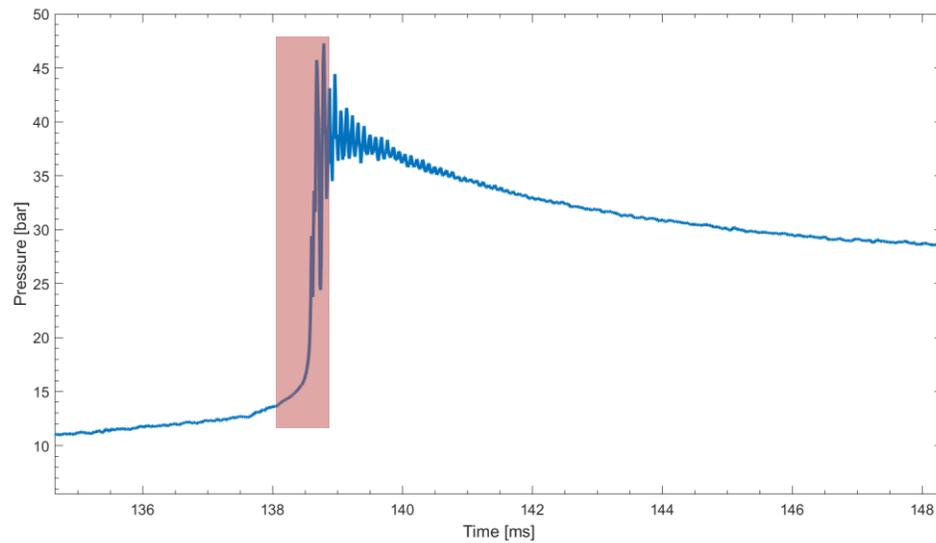
Figure 16: Pressure vs. Time Plot at 0.6/0.4 composition at 323 K which had the Shortest Ignition Time.

Box drawn shows close-up region
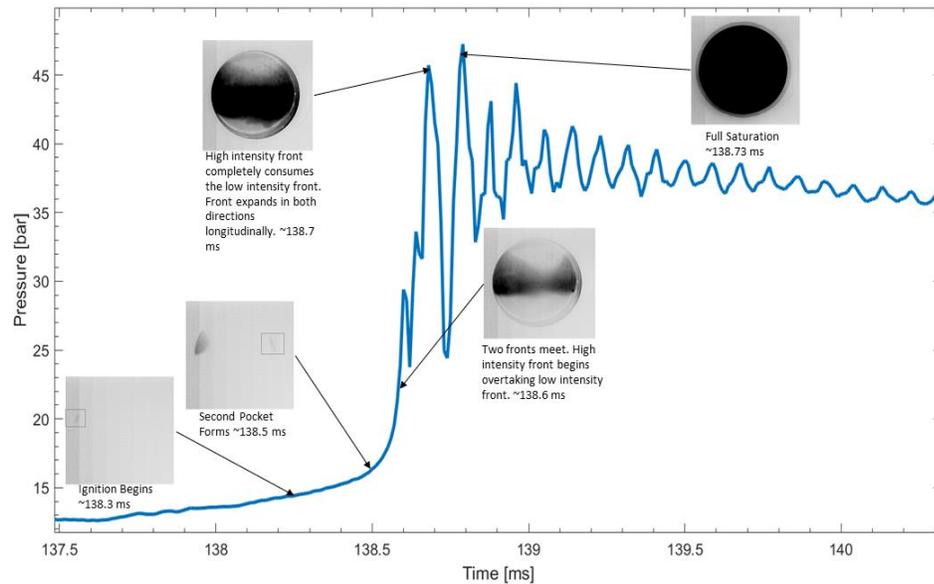
Figure 17:Close-up 0.6/0.4 Composition at 323 K Annotated with High Speed Combustion Images

Figure 17 shows the entire combustion event occurs in this case in 0.43 ms as opposed to the ~5 ms the combustion event takes in Figure 15. In addition, pressure fluctuations appear at this condition, suggesting ignition knock is present at this condition. Ignition begins higher on the cylinder for the Figure 17 case and the second front forms symmetrically, 120° away from the initial front. Again, there are two distinct fronts, a low and a high intensity front, but instead of propagating upwards, these fronts move laterally and meet, and then move longitudinally in both directions, saturating the cylinder completely only 0.13 ms after the two fronts met. While Figure 15 and Figure 17 show the two extremes of the conditions, the other cases fall in line with many of the trends. Saturation happens quicker as propane is decreased and initial temperature increased, and the combustion event happens faster under the same conditions.

A trend that is observed by only analyzing the images is that the starting location of the ignition fronts change as the composition is changed, as shown by Figure 18.
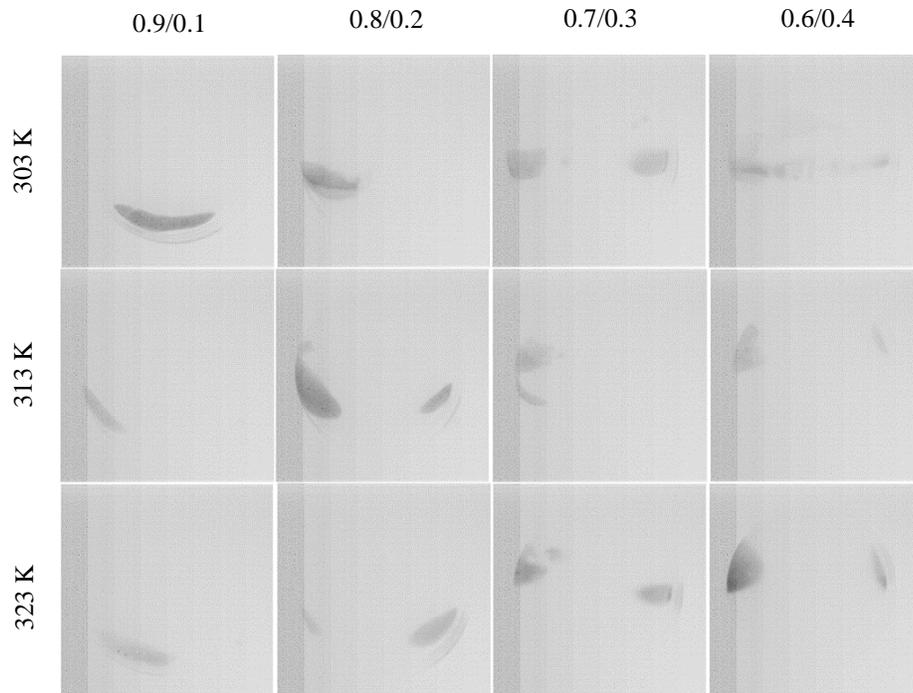
Figure 18: Ignition Start Locations

As propane is decreased, the starting location for the reaction front moves upwards along the cylinder walls. However, the ignition location along the cylinder walls is insensitive to initial temperature. Kokjohn et al. also observed ignition at the cylinder walls, and because they could measure local equivalence ratio, they suggested ignition begins at the wall because the mixture became richer the further it is from the center [24]. Figure 19 shows how Kokjohn et al.'s findings could apply to this study. Even though the equivalence ratio was kept constant in terms of fuel injection, the stratification introduced by the injection of

the HRF would vary the equivalence ratio in local pockets, with some falling below 0.6 and some above 0.6. Kokjohn et al. measured that the mixture equivalence ratio linearly increased as the measurements furthered from the center of the cylinder [24]. An example of this is displayed by Figure 19. This study does not have the data to recreate and validate what Kokjohn et al. observed, therefore Figure 19 is only a hypothetical recreation of how Kokjohn et al.'s findings could be used to explain the ignition start location. The hypothesis that the cylinder walls are at a higher compressed temperature than the cylinder center (as will be discussed later) combined with hypothesizing that that the local equivalence ratio is higher at the walls, provides a possible explanation for ignition beginning at the walls.

The aforementioned hypothesis for the wall temperature being greater than the center temperature is illustrated by Figure 20. At the time the HRF is injected, it is assumed that the wall and center temperatures are equal, and as the HRF is sprayed in, the mixture is equally cooled. However, the band heaters are placed on the cylinder walls, therefore there is a net heat flux into the mixture originating at the walls, so the wall temperature begins to rise prior to compression, making it just slightly hotter than the center as compression begins. Assuming the heat flux is restricted to the walls, therefore, the walls reach the compressed temperature required for ignition before the center region does. Again, combined Kokjohn et al.'s measurements on equivalence ratio, this may explain why ignition originates at the cylinder walls.
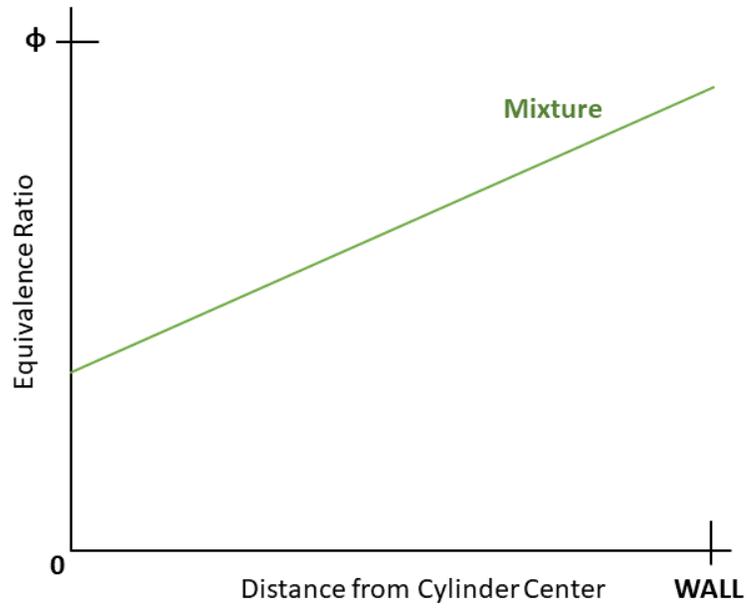
Figure 19: Local Equivalence Ratio Distribution Trend based on Kokjohn et al.'s findings. This figure only

shows a hypothetical trend.
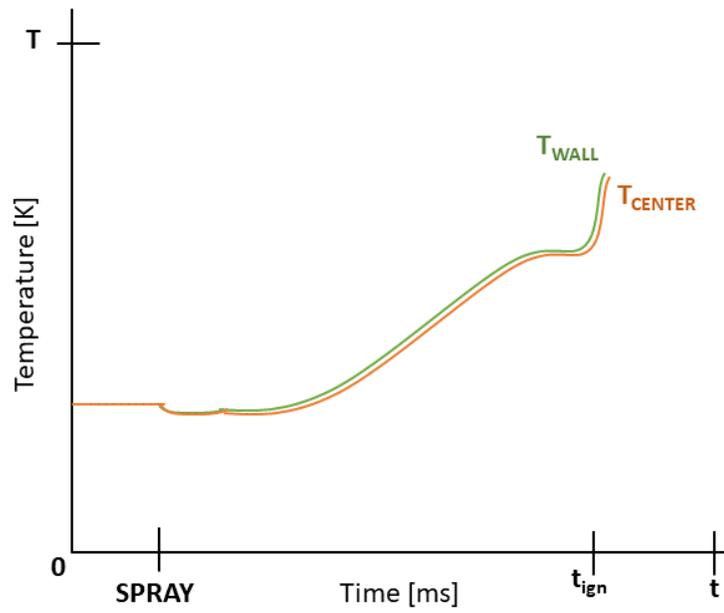
Figure 20: Hypothesized Temperature Plot at Wall and Center

As mentioned earlier, ignition also originates at higher locations along the cylinder as propane is decreased in the mixture. Figure 21 provides a possible explanation for that, where the horizontal axis is the vertical distance from the base of the cylinder and the series is the temperature distribution. The "hypothetical most reactive points" are the local *n*-heptane mole fractions that correspond with the highest reactivity of the mixture. There is an ideal coupling of local *n*-heptane mole fraction and compressed temperature condition in which the mixture is most reactive, and that couple represents the ignition condition. However, as the mixture is changed i.e. propane content decreases, the most reactive mole fraction and compressed temperature occurs at a higher location along the cylinder wall. This could be a result of the spray and evaporation dynamics of the *n*-heptane. As propane content is decreased, the *n*-heptane faces less resistance in both the motion of the spray and the evaporation motion and is able to travel higher on the cylinder walls during the five seconds of evaporation.
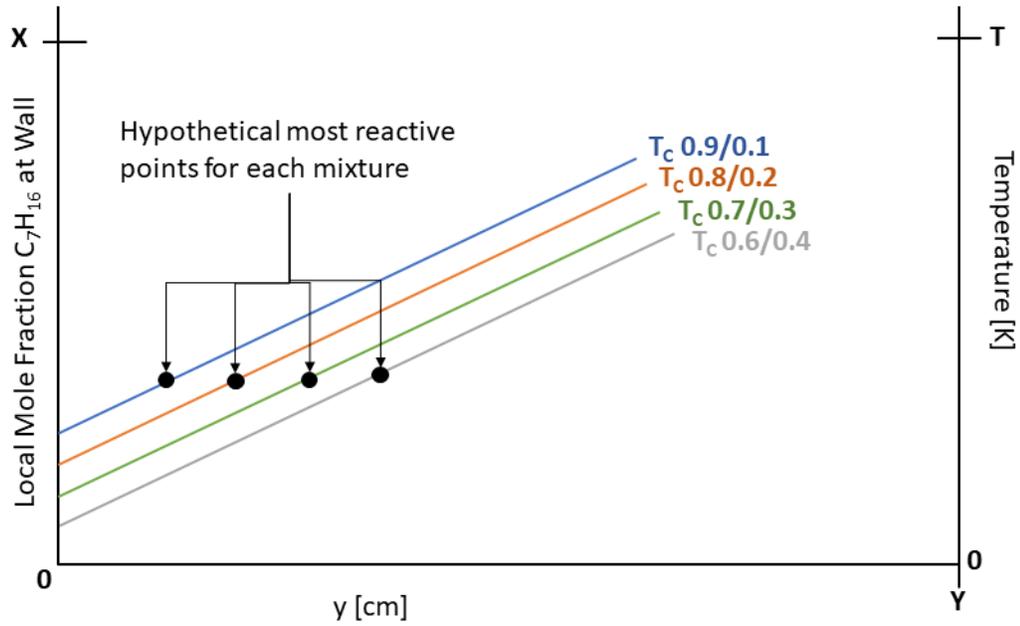
Figure 21: Temperature and Local *n*-heptane Mole Fraction vs Longitudinal Location on Cylinder Wall

3.2   Overview of Quantitative Analysis

Zeldovich and Gu et al.' s work with reaction zone growth provides an excellent way to analyze the work of this study, particularly by using Equation 10 to solve for the temperature gradient [27], [28].

$$u_a = \left(\frac{\partial \tau_i}{\partial T} \frac{\partial T}{\partial x}\right)^{-1} \tag{10}$$

For Equation 10, u_a is velocity of the reaction front, $\partial \tau_i / \partial T$ is the gradient of autoignition delay time, and $\partial T / \partial x$ is the temperature gradient. Equation 10 was utilized to solve the

temperature gradient at each condition. This was done by writing a MATLAB script to determine the reaction front speed, and by finding global ignition delay correlations to discover the gradient of autoignition. Given those two values, the temperature gradient was solved for. Equation 10 is generally utilized under a homogenous mixture, or "well-mixed" assumption for the entire mixture. Since this study is rooted in the heterogeneity of the HRF, Equation 10 potentially does not apply, however for this study, Equation 10 was used under an isotropic assumption. It was assumed for this study that the HRF is "poorly-mixed" equally in all direction. Under this assumption, the mixture is assumed to be homogeneously heterogenous.

3.3   Determining the Gradient of Autoignition

The first step in determining the autoignition gradient was to determine the ignition time for each case. This was done by having a MATLAB script that went through every frame of video and finding the average light intensity. It was discovered that in a state of no ignition, just a dark screen, MATLAB recorded and average intensity of 44-45 over the entire frame. Upon further investigation, it was discovered that an average frame intensity of 46 corresponded with the first sign of light from an ignition event and the average velocity would start to rise from there as the light from combustion became more intense frame after frame. Therefore, 46 was set as the threshold for determining the start of ignition. Since it was known that the camera starts recording at 100 ms after the test began, and every frame is 0.0334 ms after that, MATLAB simply ran through a loop until the

average intensity of the frame was above 46. The frame number of that point was saved and converted to time, and the time of the first frame with an average intensity above 46 was the ignition time for that condition.

Once t_{ign} was determined, the temperature at time of ignition, T_c, needed to be determined. To do that Equation 11 was utilized, there P_c was pressure at t_{ign}, obtained from the pressure data, and P_o was the initial pressure, and C_p was the specific heat and R_u is the universal gas constant.

$$\int_{T_0}^{T_c} \frac{C_p}{R_u T} dT = \ln\left(\frac{P_c}{P_0}\right) \qquad\qquad (11)[35]$$

The C_p/R_u was solved via the NASA polynomials and the integral was solved numerically in MATLAB at the time of t_{ign} for the corresponding T_c, therefore the T_c value corresponds to the temperature of the mixture at the point where the first image of ignition was observed by MATLAB. Even though the introduction of the n-heptane causes inhomogeneities in the mixture, to solve for the specific heat of the whole mixture, it was assumed that the mixture was homogenous in order to simplify subsequent calculations. This is obviously a deviation from the actual conditions of the experiment, however, every calculation done from this point forward reflects the homogeneous assumption. Figure 22 shows the T_c values with respect to initial temperature and mixture composition. In addition, Figure 23 shows the experimentally found t_{ign} for each calculated T_c at each mixture composition. The 0.9/0.1 condition again has the most interesting trends, because it is the only condition that reaches TDC at 323 K. The other conditions at 323 K ignite before TDC; thus, they

ignite at a lower pressure than they would have had they reached TDC, which means they would have a lower calculated T_c. For the 323 K cases, the mixtures ignite faster as propane decreased, which is why that pattern is evident in Figure 22. If the other mixtures at 323 K would have reached TDC before igniting, it can be hypothesized that they would have achieved higher temperatures than the 0.9/0.1 case at the time of ignition.
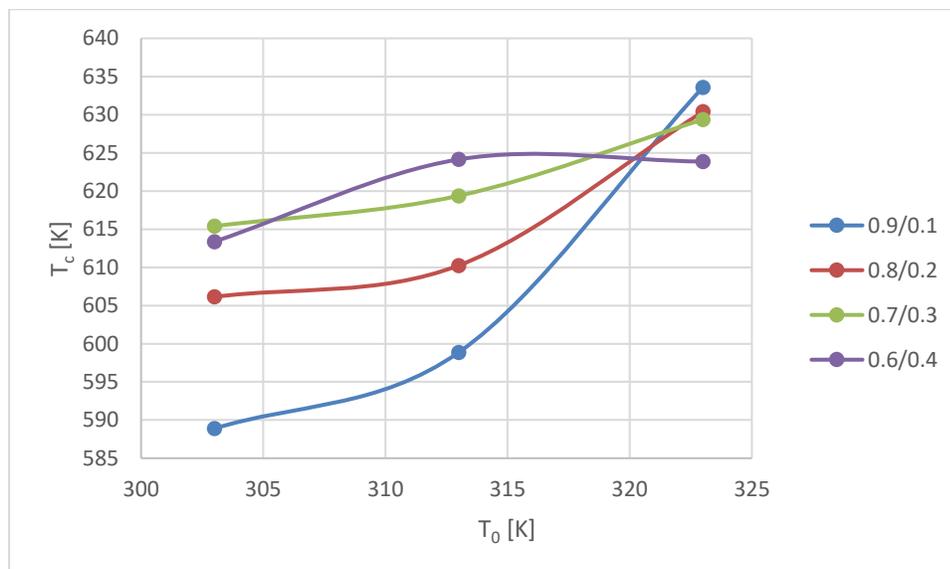
Figure 22: T_c versus T_0
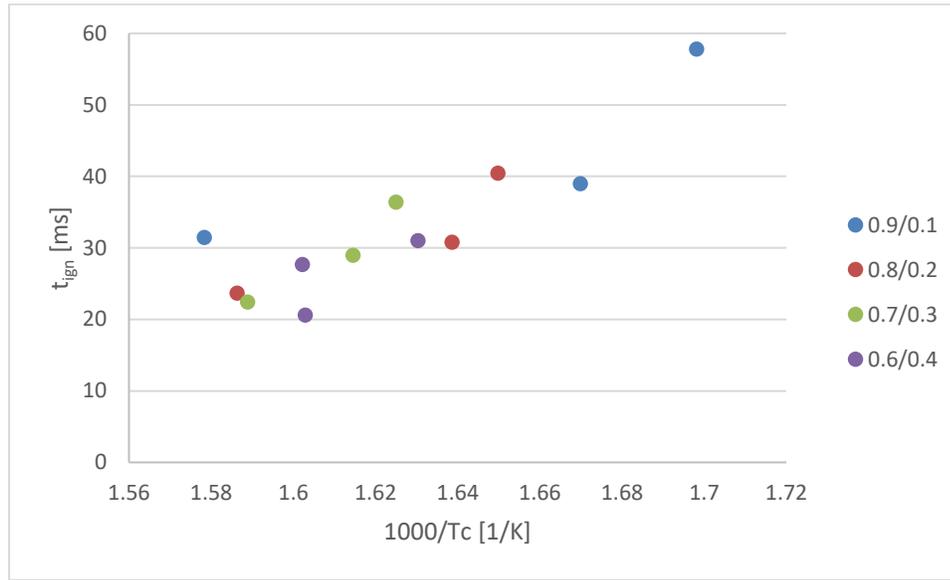
Figure 23: t_{ign} vs. T_c

Once the temperature at the start of ignition was found, a correlation to find what the theoretical ignition delay time would be if TDC was able to be reached at each condition. Equation 12 shows the Livengood-Wu predictive integral for predicting ignition delay time, where ignition delay time is represented by τ. The objective of Equation 12 is to predict the delay from the time the piston reaches TDC to the time of ignition, the definition of ignition delay time. Therefore, the use of Equation 12 in this study is an idealization, because the actual experiments did not always reach TDC, but it frames the data of this study within a metric that is commonly used in literature.

$$1 = \int_0^{\tau_{ign}} \frac{dt}{\tau(T(t),P(t))} \tag{12}[62]$$

It is also true that $\tau = Ae^{\frac{T_a}{T_c}}$ were A and T_a are optimization parameters [63]. Therefore, a MATLAB script utilizing a trial and error method to plug in the optimization parameters and utilizing the trapezoidal rule via the *trapz* function solved Equation 13 and discovered the optimized parameters for the global ignition delay correlations for all experimental cases under a homogenous assumption.

$$1 = \int_0^{\tau_{ign}} \frac{dt}{Ae^{\frac{T_a}{T_c}}} \tag{13}$$

Table 7 shows the optimization parameters for each case that were best fit to the data, and Figure 24 shows the total ignition delay time for each mixture, calculated from the optimization parameters in Table 7, where the zero point is the start of compression, ~120 ms on a pressure vs. time plot.

Table 7: Ignition Delay Correlation Parameters for Each Mixture Composition

	A	T_a [K]
0.9/0.1	1.26E-06	10100
0.8/0.2	2.51E-05	8100
0.7/0.3	2.00E-05	8100
0.6/0.4	1.26E-05	8000
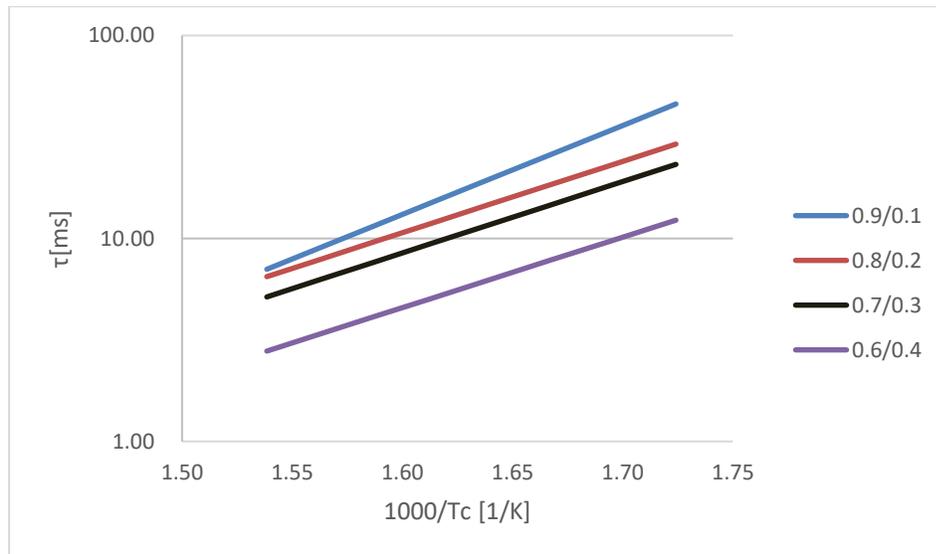
Figure 24: Global Ignition Delay Correlations for Each Mixture Composition

It is difficult to compare Figure 23 to Figure 24 because many cases to not reach TDC experimentally, however, Figure 24 provides the basis to evaluate the experiments in terms

consistent with literature. In addition, in choosing the optimization parameters the tests that did reach TDC were used as the data in which the idealized ignition delay times from Equation 12 were fit to. In some conditions, the global correlation predicts that ignition delay to be over 100 ms less than the nonhomogeneous time of ignition. Furthermore, the 0.9/0.1 case displays a larger difference with the other mixtures with a 2000 K difference in the T_a value over the other cases.

Finally, once the global ignition delay correlation was discovered for each mixture, the autoignition gradient could be found by simply taking the derivative of the global τ with respect to temperature. Equation 14 shows the gradient of autoignition and Figure 25 shows the relationship between the autoignition gradient, propane mole fraction, and initial temperature.

$$\frac{\partial \tau}{\partial T} = \frac{-AT_a e^{\frac{T_a}{T_c}}}{T_c^2} \tag{14}$$
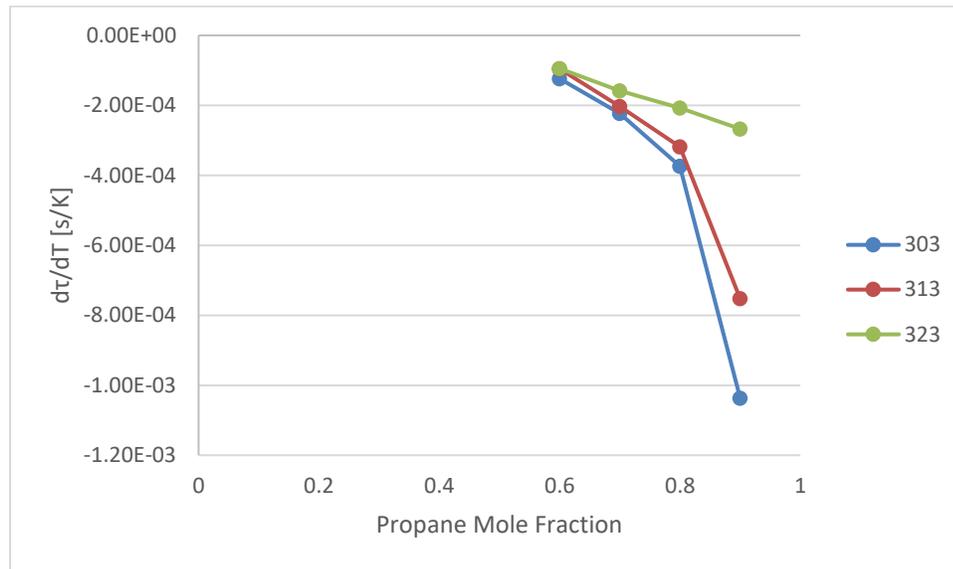
Figure 25: Autoignition Gradient vs Composition and Initial Temperature

Figure 25 shows a convergence at the 0.6/0.4 case for the autoignition gradient, implying that as propane is decreased in the mixture, initial temperature loses its effect on the autoignition gradient. Furthermore, the effect of composition is more significant for the 303 K and 313 K cases than for the 323 K cases. Figure 26 shows a CHEMKIN simulation that was performed in order to gain insight on the temperature sensitivity of each mixture. For this simulation, a constant volume reactor was chosen, and the mixture was assumed homogenous for ease of simulation.
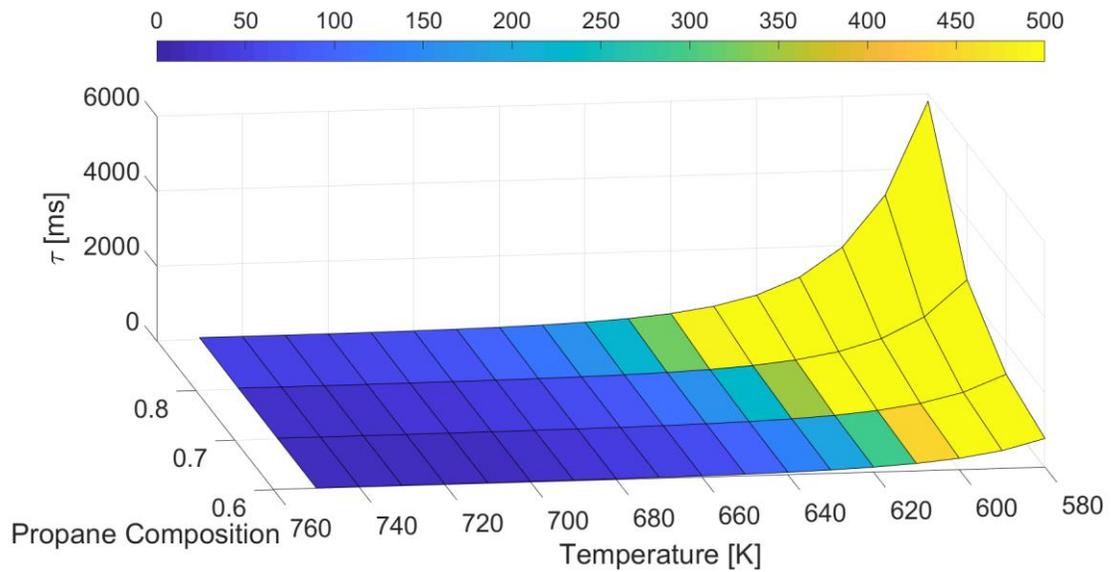
Figure 26: CHEMKIN Simulation Results on Mixture Sensitivity to Temperature

The results of the simulation appear to confirm the results of the autoignition gradient. Ignition time temperature sensitivity increases as the propane content of the mixture increases. Therefore, once the autoignition gradient was found, the reaction front speed could be determined to solve for the temperature gradient.

3.4   Reaction Front Speed

3.4.1   Determining Reaction Front Speed

First, since the autoignition gradient was governed by the phenomena happening up to and at the start of ignition, it was assumed that only the initial velocity was relevant for these calculations. Therefore, the initial velocity for this case was defined as the average

reaction front velocity of the first three frames, which corresponds with the velocity at 0.1 ms after ignition has started. To accomplish this a MATLAB script was written to identify the locations of the leading edge of the reaction front in the first three frames after ignition. Since every case has a different starting point for ignition, the code had to identify and locate the leading edge of the front regardless of where ignition began. The first step to accomplish is identifying the center of the cylinder and the cylinder walls. It was discovered that when the cylinder was fully saturated, the average intensity of a fully saturated image was between 165 and 175. This was a parameter that had to be tuned for each test, however once that threshold was reached, an image, as seen by Figure 27, was shown the user of the code to verify that the cylinder was saturated.

Figure 27: Full Cylinder Saturation

Since all the frames were 256 x 256 pixels, MATLAB interpreted each frame as a 256 x 256 matrix of intensities, and therefore it was assumed that the center point for the cylinder would be near th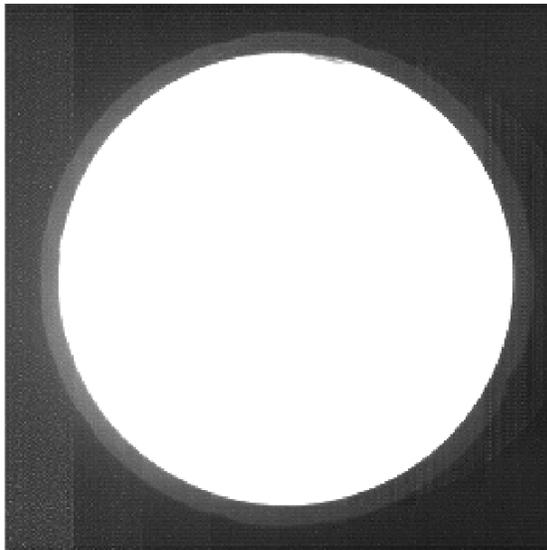e point (128,128), which proved to be a decent assumption as a starting point, based on the actual center points that were found. Furthermore, the highest intensity value, which is shown by the white light in Figure 27, is 255, therefore the edges of the of the cylinder were represented by locations where the light intensity was less than 250. Therefore, starting at the assumed center point, a *for* loop in MATLAB found the top, bottom, right, and left edges at the first point in each direction below an intensity of 250. Then the center point was adjusted so that the distance from top to center and bottom to center was equal, and the distance from left to center and right to center was equal. This was done automatically by MATLAB by shifting the center point. For example, for the case shown in Figure 27 the center point of the cylinder was found to be (129, 132).

Next, even though the cylinder is physically circular, using the light to find many points to make a perimeter, leads to a circular assumption being to much of an idealization, small ways in which the light distorts the actual shape in the image. Therefore, when finding the perimeter points all along the edges of the cylinder, it was assumed the cylinder was an ellipse, because all circles are ellipses, so if there were a case of a perfect circle in an image, it would be treated correctly. However, since not all ellipses are circles, the opposite treatment would not work. Using the range of angles, θ, [0 2π] with an interval of π/144, the coordinates for points that lie on the perimeter of the cylinder ellipse were found by using Equation 15 and Equation 16.

$$x = \pm \frac{ab}{\sqrt{b^2 + a^2(tan\theta)^2}} \tag{15}$$

$$y = \pm \frac{ab}{\sqrt{a^2 + \frac{b^2}{(tan\theta)^2}}} \tag{16}$$

The variables a and b are the longitudinal and lateral radii of the ellipse, respectively. Once all of the points were found, Figure 28 would be displayed by the code to verify that the perimeter found was reasonable.
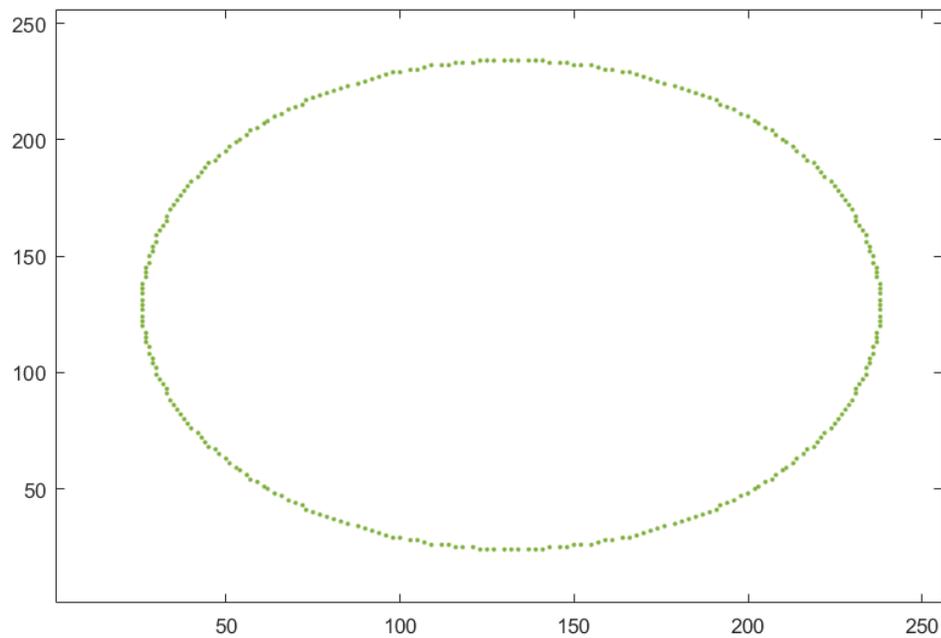
Figure 28: Cylinder Perimeter Points

Therefore, now that the center points and 289 points representing the cylinder walls were found, the next step of the code was to go frame by frame and search for signs of intensity, signaling a front, and locating the leading edge of the front.

As previously discussed, the challenge in accomplishing this was that ignition begins in a different location for almost every test condition. However, it is known that ignition always began at the wall of the cylinder. Therefore, the strategy was to have nested *for* loops in the code report back the intensity of each cell, while moving in a spiral direction from the center, illustrated by Figure 29. It was assumed that in a spiral fashion, the first point above the set intensity threshold that the spiral came in contact with would be the leading edge of the initial reaction front.

Figure 29: Spiral Beginning at the Center. The nested loops would check the luminosity values of the cells in this shape to find the first instance of a front propagating from the cylinder wall. However, once the radius of the spiral surpassed the larger ellipse radius, the code reported no front found, and moved on to the next frame

This spiral process would start 10 frames before the frame corresponding with t_{ign} and 5 frames after in order to capture everything concerning the start of ignition, and the first three frames that showed reaction front movement were analyzed for velocity data. Furthermore, to establish the threshold, the matrix corresponding with the frame being analyzed was subtracted from the matrix corresponding with the very first frame of the video, where no ignition is occurring. This rids the analyzed frame of background light and allows for the only increase in light to come from the actual ignition front. Therefore, since the base light threshold was decreased to being less than 10, the code identified the leading edge of a front as the first point in which intensity was recorded as being 15 or greater. When that point was found, the code saved the coordinates and went to the next frame. In addition, the code would display images to the user that defined which front, in the case of multiple fronts, was being analyzed. For all these cases, the it was verified that the first front formed was the only front that was analyzed.

Since many of the beginning frames analyzed saved a zero, the first three non-zero numbers saved by the codes were used to find the initial velocity. The velocity at each frame was found by taking the change in leading edge displacement from one frame to the frame previous divided by the change in time. Then the three velocities were averaged, yielding an initial average velocity. Finally, the units were converted from pixels/second to cm/second. These velocities were found for each test of each case and were then available to be used, along with the autoignition gradient, to find the temperature gradient.

The relationships between the initial velocity and various other parameters do provide some interesting insight into the behavior of the mixtures. Figure 30 shows the

relationship between the initial velocity and initial temperature. The point circled in red in Figure 30 and Figure 31 is highlighted because it is only based on one data point, despite the condition having been tested three times. During data analysis, the other two tests at that condition were deemed unusable because they fell massively outside acceptable range of standard deviation.
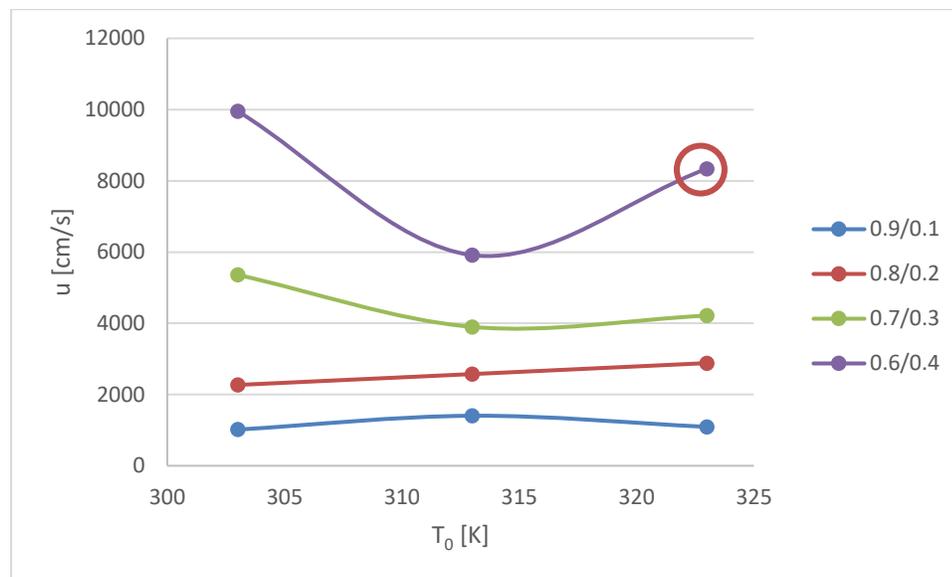
Figure 30: Initial Front Velocity vs. Initial Temperature

The first observation is that front speed increases as propane content decreases. This is expected as *n*-heptane is the more reactive fuel, therefore the more *n*-heptane there is, the faster the reaction front will move. Furthermore, the initial temperature appears to play no role in the front velocity for the 0.9/0.1 and 0.8/0.2 cases, but there does seem to be a relationship between initial temperature and front velocity for the other two cases of lower

propane content. Expanding the relationship between front speed and temperature, Figure 31 shows the relationship between front speed and T_c.
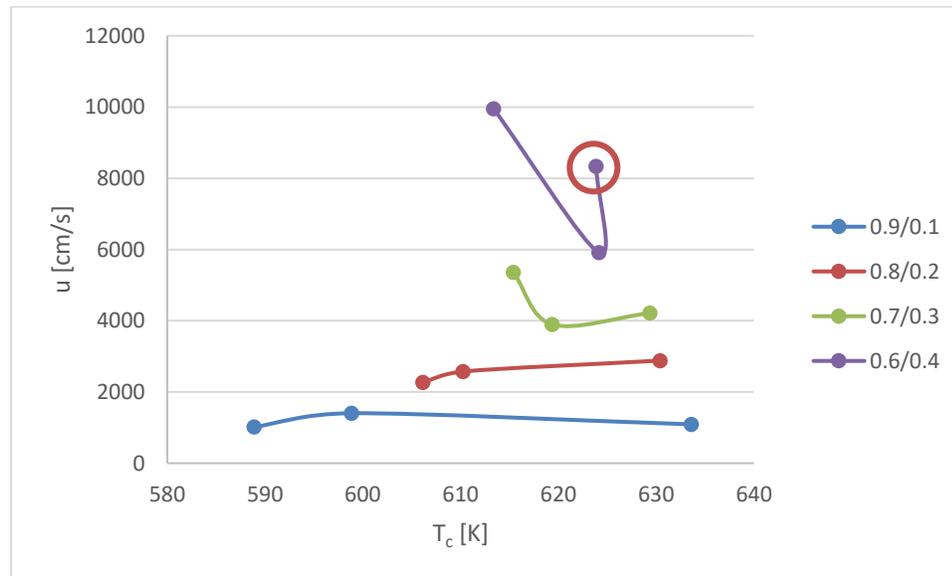
Figure 31: Initial Front Velocity vs T_c

Again, front speed at the two higher propane cases seem unaffected by T_c, but for the two lower propane cases T_c has a large influence. The 0.7/0.3 and 0.6/0.4 case both exhibit behavior that suggests that whose cases lie within the negative temperature coefficient (NTC) region, or that those conditions experience more severe stratification. However, since the 0.6/0.4 at 323 K data point is only based on a single test, it is hard to say definitively what governs that behavior or if that behavior is accurate. It should be noted however that the 0.7/0.3 at 323 K case is based on multiple test points, and it does exhibit similar behavior to the 0.6/0.4 at 323 K case. Finally, Figure 32 shows the relationship between initial front speed and mixture composition.
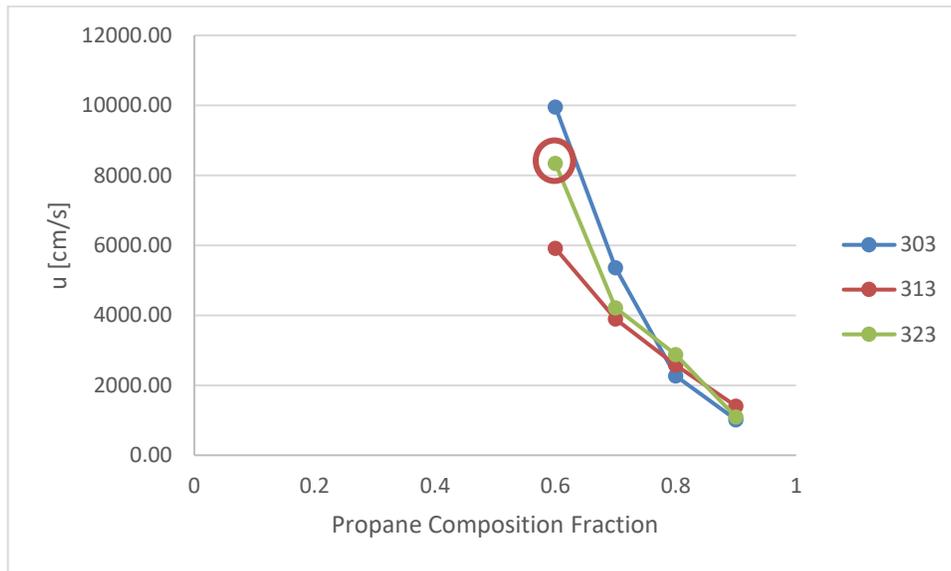
Figure 32: Initial Front Velocity vs Mixture Composition

Initial velocity converges at the 0.9/0.1 case showing again that front speed at the 0.9/0.1 case occurs independent of temperature. However, as propane is decreased in composition, it is clear that temperature plays a larger and larger role in the initial front speed. As in Figure 30 and Figure 31 there is the issue of the 0.6/0.4 at 323 K data point being based on only one test. Again, the non-monotonic behavior shown by Figure 32 could be due to the condition lying in the NTC region or due to more extreme stratification at that point. However, more experimentation would need to be done to definitively make a conclusion about the non-monotonic behavior between temperature and reaction front speed.

3.4.2 Using Intensity Data to Solve for Velocity

Another MATLAB script was written during this process to track intensity throughout the frames of the videos. The hypothesis was that the time derivative of the intensity could be a replacement for finding the wave speed. The average initial intensity after ignition, the number of initial low intensity cells ($15 > $ Intensity $ > 200$), and the number of initial high intensity cells (Intensity $ > 200$) were the three ways the intensities were measured. Plots of these metrics are shown by the following four figures. Figure 33 shows the average intensity and low intensity traces in time for the 0.9/0.1 case with varying temperatures. The peak of the number of low intensity cells represents the point in which the high intensity front forms and as the high intensity front propagates, the number of low intensity cells decrease, until combustion ends. At the end of combustion, the number of low intensity cells increase again. Figure 33 shows a split between the average intensity and the number of low intensity cells that is sensitive to initial temperature. For all three temperatures, the number of low intensity cells grows at a faster rate than the average intensity, but the difference in growth rate decreases as initial temperature decreases. This suggests that the low intensity front propagates faster at higher initial temperatures.

Figure 33: Average Intensity and Number of Low Intensity Cells versus Time for the 0.9/0.1 Case with

Varying Temperatures

Figure 34: Average Intensity and Number of Low Intensity Cells versus Time at 303 K for Varying

Mixture Composition

To explore the effect composition had on the difference in slope of the average intensity trace and the number of low intensity cells, Figure 34 was analyzed. The effect of composition only applies to the 0.9/0.1 case. The other three cases show remarkably similar slopes, which suggests an insensitivity of the low intensity front propagation to changes in mixture composition unless the fuel mixture is 90% propane. Figure 35 shows the relationship between the average intensity and number of high intensity cells in time at the 0.9/0.1 case with varying temperatures. The same temperature sensitivity exists as with the low intensity front, as temperature decreases, the difference in slope decreases.
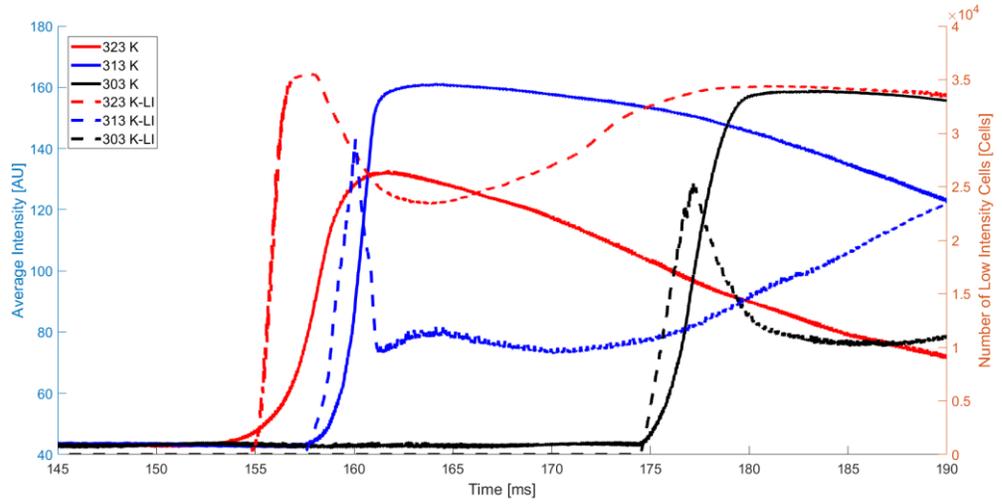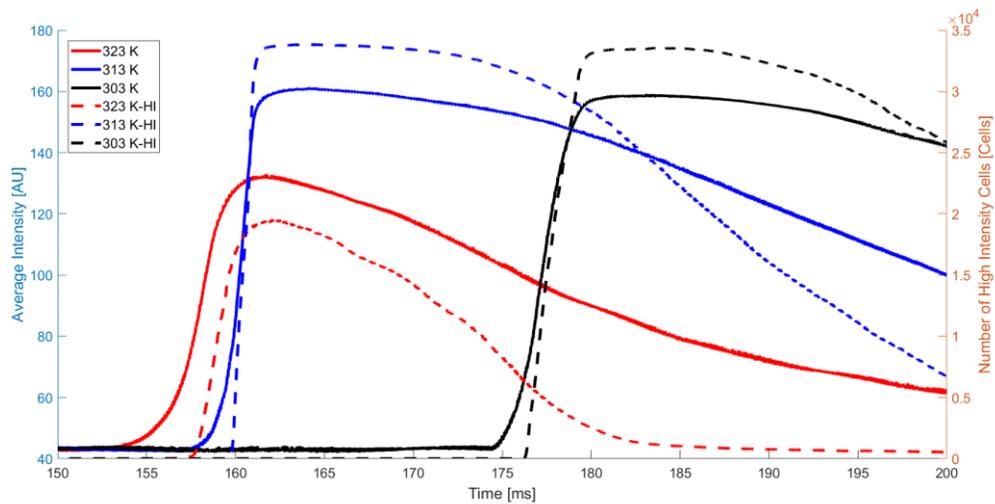

Figure 35: Average Intensity and Number of High Intensity Cells versus Time for the 0.9/0.1 Case with Varying Temperatures
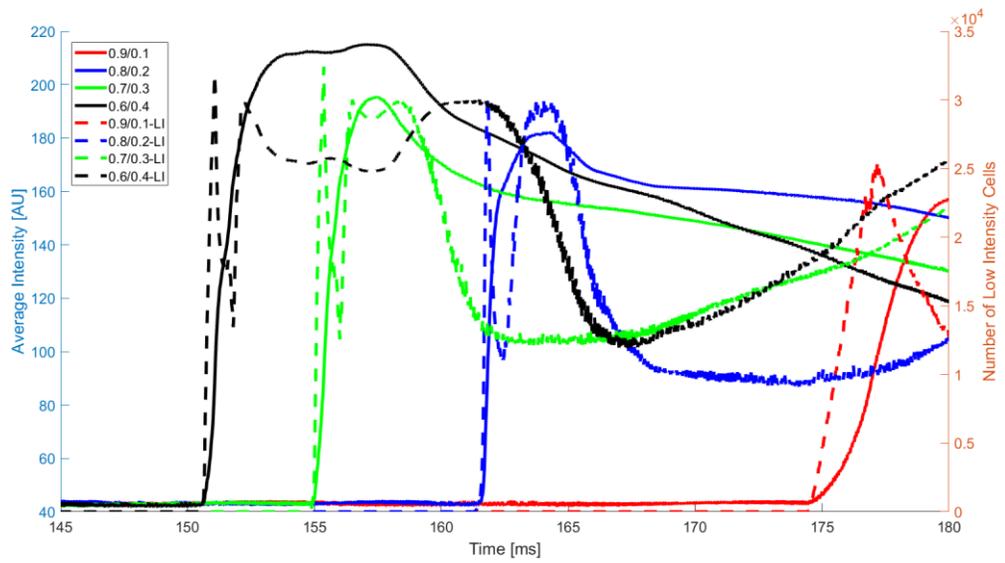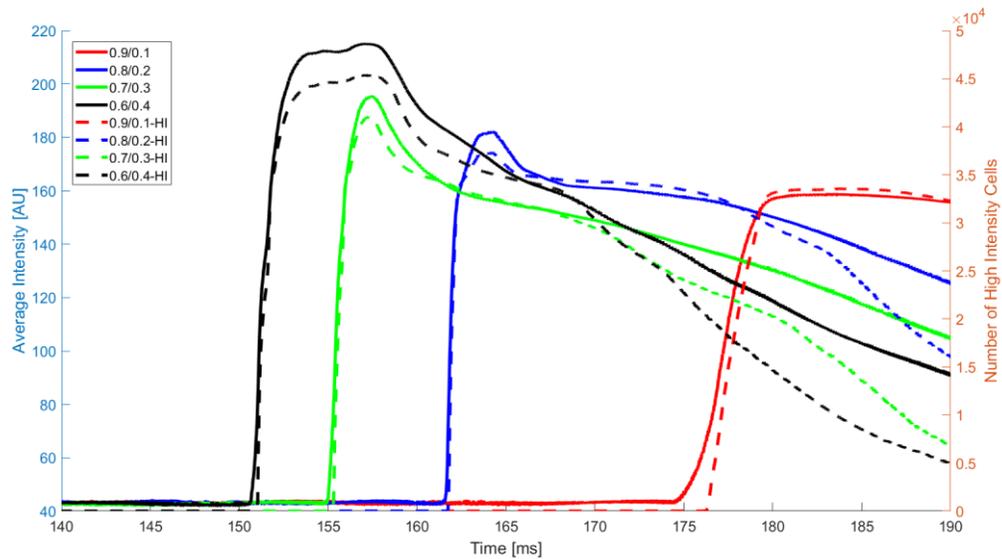
Figure 36: Average Intensity and Number of High Intensity Cells versus Time at 303 K for Varying

Mixture Composition

Figure 36 further shows that while at the difference in slope is sensitive to composition at

the 0.9/0.1 case, there is far less compositional sensitivity when comparing the slope of the

average intensity curve to the slope of the number of high intensity cells curve, than there

is when comparing to the slope of the number of low intensity cells curve.

The analysis of the slope raised the question of whether the intensity plots could be

used to make conclusions about initial front speed. In order to compare to velocity, these

metrics were treated as similar to the displacement of the reaction front and a derivative

with respect to time was taken of these metrics. Figure 37 shows the time derivative of

initial average intensity versus mixture composition, Figure 38 shows the time derivative

of initial number low intensity cells versus mixture composition, and Figure 39 shows the

time derivative of initial number high intensity cells versus mixture composition.
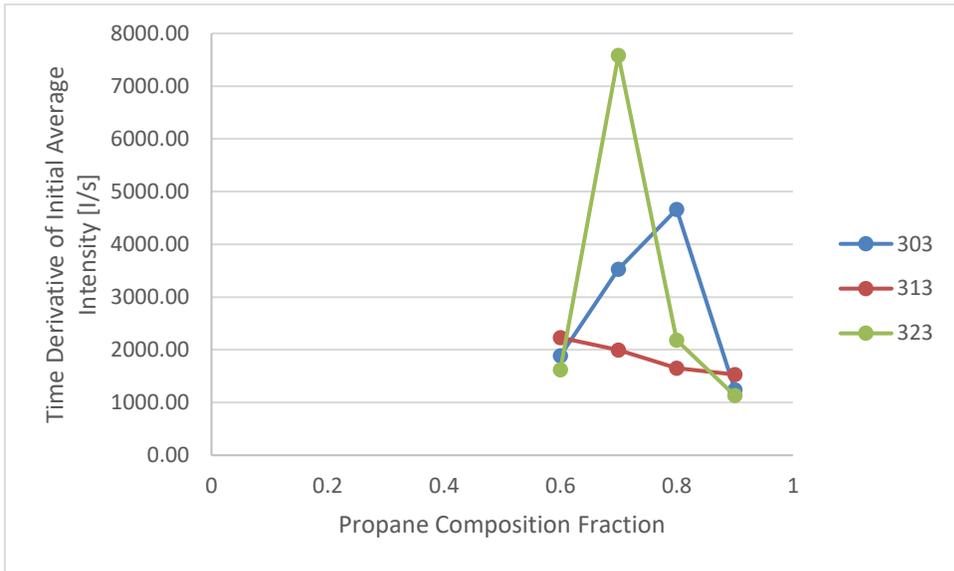
Figure 37: Time Derivative of Initial Average Intensity vs. Mixture Composition
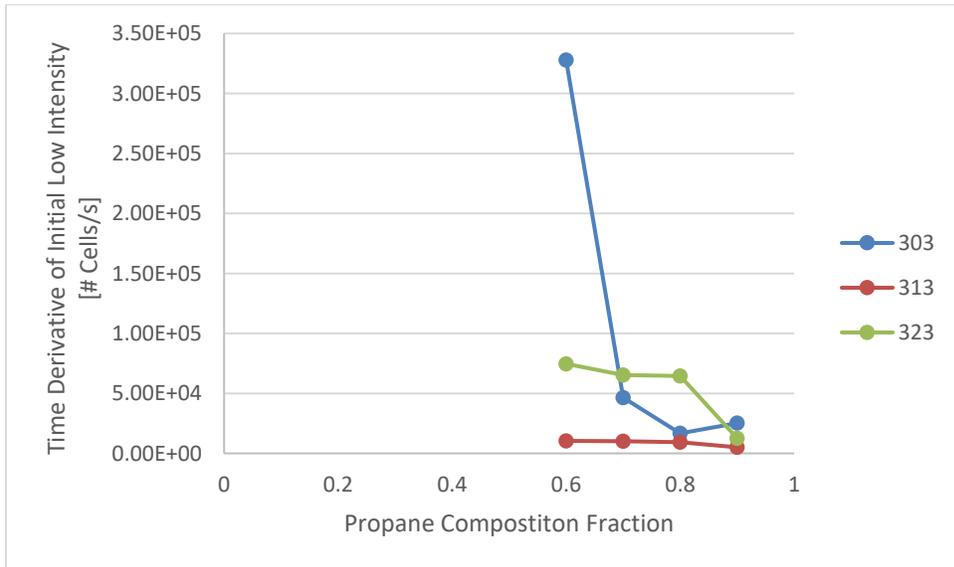
Figure 38: Time Derivative of Number of Initial Low Intensity Cells vs. Mixture Composition
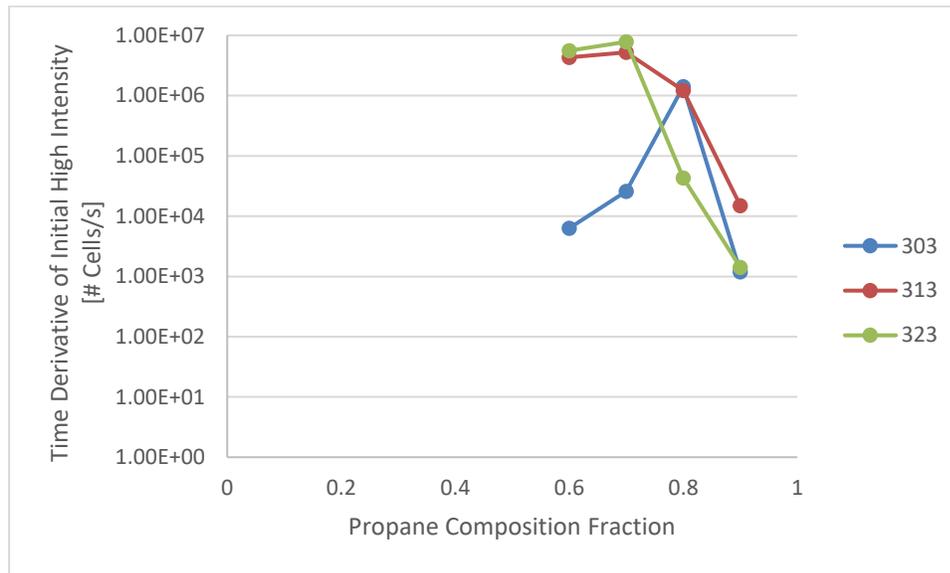
Figure 39: Time Derivative of Initial Number of High Intensity Cells vs. Mixture Composition

The time derivative of the intensity metrics do not closely follow the initial velocity trends. The most probable reason for this is that the growth of intensity occurs over an area, therefore a metric of "time derivative of number of cells" should be treated as more closely related to area changes with respect to time and not displacement changes with respect to time. However, all three metrics still display a convergence at the 0.9/0.1 case. Even the high intensity metric shows the 0.9/0.1 convergence, even though the high intensity cells do not occur until after the low intensity front has been developed, and has a further connection from the initial velocity than the average intensity and low intensity metrics do. Therefore, while the time derivative of intensity cannot be assumed to be related to, or used as a replacement to, actual front velocity, it does suggest that RZG at the 0.9/0.1 case may be independent of temperature, as seen previously by the actual wave speed data.

3.5   Temperature Gradient

Now that the initial reaction front velocity and the autoignition gradient are known, Equation 10 can be solved algebraically for the temperature gradient. Figure 40 shows the temperature gradient, $\partial T / \partial x$, with respect to mixture composition.
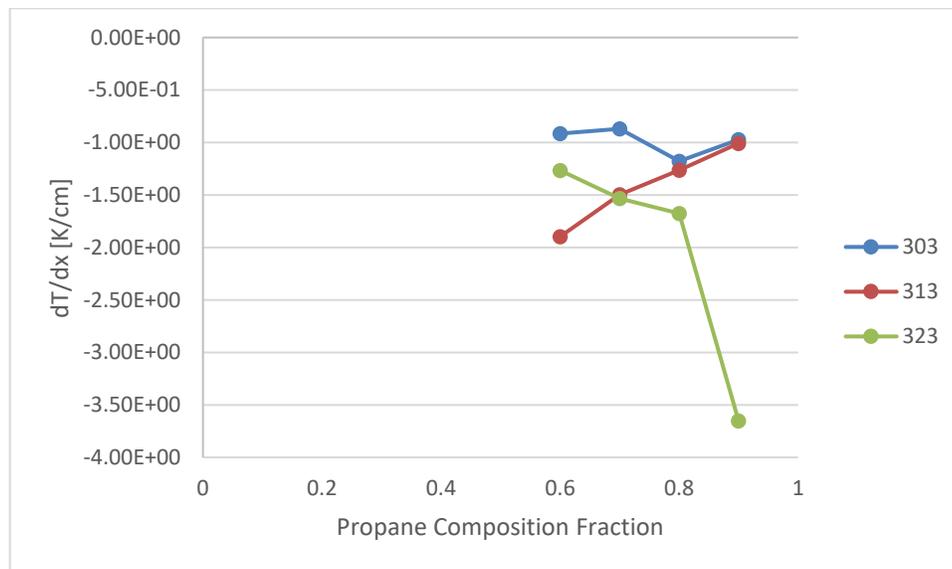
Figure 40: Temperature Gradient vs. Mixture Composition

Overall, Figure 40 shows that there is not a large temperature gradient across any cases. Literature shows that often times temperature gradients are on the order of 5 K/mm, whereas the data from this study shows temperature gradients form 0.1 K/mm to 0.3 K/mm [64], [65]. This could be a result of the fact that to simplify this analysis local inhomogeneities were not taken into account, only the global inhomogeneity. Figure 41 shows hypothetical mass fraction and temperature combinations that might be more

realistic in the cylinder. If the actual diffusion in space curve could have been known, as Figure 41 illustrates, combinations, represented by the red boxes, of fuel mass fraction and temperature could have been obtained at multiple locations and used to find a range of specific heats. Under the idealized calculations, only the injected mass fractions and global initial temperature were considered in the specific heat calculations, but had the local mass fractions and temperatures been known throughout the mixture, a range of temperature gradients could have been calculated from the range of calculated specific heats. This could then either confirm the small temperature gradient or give reason to suspect a larger temperature gradient was present.
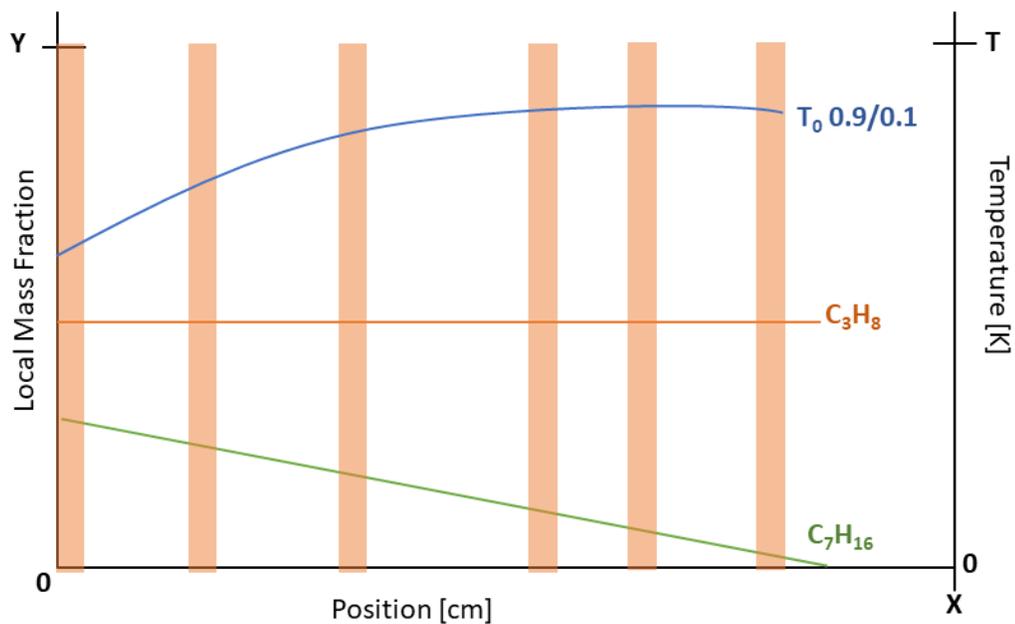
Figure 41: Hypothetical Heterogeneous Combinations of Fuel Mass Fraction and Temperature

4. CONCLUSIONS AND FUTURE WORK

4.1 Conclusions

The objective of this study is to utilize fuel octane number stratification combustion strategy to optically observe the influence of the low-reactivity fuel, propane, on the dynamics of the reaction zone growth. The majority of the conclusions drawn from this data stem from the qualitative analysis of the pressure traces and high-speed imaging.

- As propane content was increased in the mixture, ignition time increased.

- As initial temperature was decreased, ignition time increased.

- The origin location of the reaction front(s) move upwards on the cylinder as propane composition is decreased, but front origin location is insensitive to initial temperature changes.

- As propane content is decreased, the autoignition gradient develops an insensitivity to initial temperature, which corresponds to an idealized, homogeneous constant volume chamber CHEMKIN study on the relationship between ignition delay and temperature.

- As propane content decreases, reaction front speed increases.

- Reaction front speed for the 0.9/0.1 and 0.8/0.2 case displays an insensitivity to initial temperature and compressed temperature at the time of ignition.

- Reaction front speed for the 0.7/0.3 and 0.6/0.4 case do suggest initial and compressed temperature sensitivity and further experimentation would reveal the extent of the sensitivity.

- Time derivatives of initial luminous intensity values cannot be used as a surrogate for finding initial reaction front velocity.

4.2   Future Work

Based on the work presented in this thesis, there are a few options for future work, along with a few equipment improvements that should be made. First, to continue RCCI in an RCM work, an electronic valve to release the hydraulic oil to start an RCM test should be involved. This valve would be controlled in by a LABVIEW VI. In addition, the injection of the HRF should be controlled by the same LABVIEW VI. Under the current condition, there is opportunity for error on the timing of the HRF stratification because the hydraulic stop is manually released after a 5 second timer, that is manually set, goes off. Additionally, an electronically controlled valve could decrease the HRF mixing time. For example, a 1 second mixing time is essentially impossible under manual fuel injection, timer start, and hydraulic release conditions. However, in a system where a user predefines the HRF mixing time, a LABVIEW VI could be started where it would inject the fuel, pause for the user defined time, and then release the hydraulic stop and run the test. Furthermore, a sapphire or quartz window would expand the image data that could be achieved from testing, in addition to a higher tech image capturing device. Obviously,

updating the high-speed camera and acquiring different windows can be extremely expensive, so those are more hopeful dreams than necessities to further the work.

In addition to updating the equipment, there are a few other ways to expand the work of this thesis. As mentioned, varying the HRF mixing time would be an entirely new variable to study. The author had done that work before work on this study began. Previously the author allowed the HRF to mix for 5, 30, 60, and 120 seconds before realizing that any time after 5 seconds was too long to reasonably prove mixture inhomogeneity. However, the addition of the electronic valve could allow for mixing times of less than 5 seconds, which could potentially show interesting data. In addition, different LRF fuels should be tested. There are a number of engine companies developing heavy duty propane engines, but also natural gas and hydrogen engines [66], [67]. Hydrogen and natural gas have a RON of approximately 130 which makes it means it has lower reactivity than propane, but both are viable alternative fuels, and are not oil-based. First, broadening the study to include other LRFs increases the relevancy of future studies by keeping in step with industry. In addition, exploring a range of octane number stratification i.e. 100 vs 0, 110 vs 0, and 130 vs 0, may unveil new trends and addition explanations for previously exposed trends seen by this study and others.

BIBLIOGRAPHY

[1]   S. Onishi, S. H. Jo, K. Shoda, P. Do Jo, and S. Kato, "Active Thermo-Atmosphere Combustion (ATAC) - A New Combustion Process for Internal Combustion Engines," in *SAE Technical Paper Series*, 1979, vol. 1, no. 1979, pp. 1851–1860.

[2]   M. Noguchi, Y. Tanaka, T. Tanaka, and Y. Takeuchi, "A Study on Gasoline Engine Combustion by Observation of Intermediate Reactive Products during Combustion," in *SAE Technical Paper Series*, 1979, vol. 1, no. 1979, pp. 2816–2828.

[3]   P. M. Najt and D. E. Foster, "Compression–Ignited Homogeneous Charge Combustion," *SAE Pap.*, vol. 92, no. 1983, p. 830264, 1983.

[4]   J. E. Dec, Y. Yang, and N. Dronniou, "Boosted HCCI - Controlling Pressure-Rise Rates for Performance Improvements using Partial Fuel Stratification with Conventional Gasoline," vol. 4, no. 1, 2018.

[5]   J. E. Dec, "Advanced compression-ignition engines — understanding the in-cylinder processes," *Proc. Combust. Inst.*, vol. 32, no. 2, pp. 2727–2742, 2010.

[6]   S. Turns, "An Introduction to Combustion Concepts and Applications," 2012.

[7]   J. E. Dec, W. Hwang, and M. Sjöberg, "An Investigation of Thermal Stratification in HCCI Engines Using Chemiluminescence Imaging," vol. 2006, no. 724, 2006.

[8]   M. Sjöberg, J. E. Dec, and N. P. Cernansky, "Potential of Thermal Stratification and Combustion Retard for Reducing Pressure-Rise Rates in HCCI Engines, Based on Multi-Zone Modeling and Experiments," vol. 2005, no. 724, 2005.

[9]   R. E. Herold, J. M. Krasselt, D. E. Foster, J. B. Ghandhi, D. L. Reuss, and P. M. Najt, "Investigations into the Effects of Thermal and Compositional Stratification on HCCI Combustion – Part II: Optical Engine Results," *SAE Int. J. Engines*, vol. 2, no. 1, pp. 2009-01–1106, 2009.

[10]   O. T. Lim, H. Nakano, and N. Ilda, "The Research About the Effects of Thermal Stratification on n-Heptane/iso-Octane-Air Mixture HCCI Combustion Using a Rapid Compression Machine," *SAE Tech. Pap. Ser.*, no. 2006-01–3319, pp. 776–790, 2006.

[11]   H. Nakano, O. T. Lim, and N. Iida, "An Investigation of the Effect of Thermal Stratification on HCCI Combustion by using Rapid Compression Machine," *SAE Tech. Pap. 2007-01-1870*, vol. 116, no. 2007, pp. 364–374, 2007.

[12]   C. Strozzi, A. Mura, J. Sotton, and M. Bellenoue, "Experimental analysis of propagation regimes during the autoignition of a fully premixed methane-air mixture in the presence of temperature inhomogeneities," *Combust. Flame*, vol. 159, no. 11, pp. 3323–3341, 2012.

[13]   K. Inagaki, T. Fuyuto, K. Nishikawa, K. Nakakita, and I. Sakata, "Dual-Fuel PCI Combustion Controlled by In-Cylinder Stratification of Ignitability," vol. 2006, no. 724, 2006.

[14]   M. Sjöberg and J. E. Dec, "Smoothing HCCI Heat-Release Rates Using Partial Fuel Stratification with Two-Stage Ignition Fuels," vol. 2006, no. 724, 2006.

[15]   R. M. Hanson, S. L. Kokjohn, D. A. Splitter, and R. D. Reitz, "An Experimental Investigation of Fuel Reactivity Controlled PCCI Combustion in a Heavy-Duty Engine," vol. 3, no. 1, pp. 700–716, 2010.

[16] D. Splitter, S. Kokjohn, K. Rein, R. Hanson, S. Sanders, and R. Reitz, "An Optical Investigation of Ignition Processes in Fuel Reactivity Controlled PCCI Combustion," vol. 3, no. 1, pp. 142–162, 2010.

[17] A. García, J. Benajes, M. Vanvolsem, S. Molina, and E. Belarte, "An investigation on RCCI combustion in a heavy duty diesel engine using in-cylinder blending of diesel and gasoline fuels," *Appl. Therm. Eng.*, vol. 63, no. 1, pp. 66–76, 2013.

[18] R. Hanson, S. Kokjohn, D. Splitter, and R. D. Reitz, "Fuel Effects on Reactivity Controlled Compression Ignition (RCCI) Combustion at Low Load," *SAE Int. J. Engines*, vol. 4, no. 1, pp. 394–411, 2011.

[19] S. Kokjohn, R. Hanson, D. Splitter, J. Kaddatz, and R. Reitz, "Fuel Reactivity Controlled Compression Ignition (RCCI) Combustion in Light- and Heavy-Duty Engines," vol. 4, no. 1, 2011.

[20] D. Splitter, M. Wissink, D. DelVescovo, and R. D. Reitz, "RCCI Engine Operation Towards 60% Thermal Efficiency," *SAE Tech. Pap. Ser.*, vol. 1, no. X, 2013.

[21] D. Splitter, R. Hanson, S. Kokjohn, and R. D. Reitz, "Reactivity Controlled Compression Ignition (RCCI) Heavy-Duty Engine Operation at Mid-and High-Loads with Conventional and Alternative Fuels," *SAE Tech. Pap. Ser.*, vol. 1, no. Ci, 2011.

[22] R. D. Reitz and G. Duraisamy, "Review of high efficiency and clean reactivity controlled compression ignition (RCCI) combustion in internal combustion engines," *Prog. Energy Combust. Sci.*, vol. 46, pp. 12–71, 2015.

[23] S. L. Kokjohn *et al.*, "Experiments and Modeling of Dual-Fuel HCCI and PCCI Combustion Using In-Cylinder Fuel Blending," vol. 2, no. 2, pp. 24–39, 2010.

[24] S. L. Kokjohn, M. P. B. Musculus, and R. D. Reitz, "Evaluating temperature and fuel stratification for heat-release rate control in a reactivity-controlled compression-ignition engine using optical diagnostics and chemical kinetics modeling," *Combust. Flame*, vol. 162, no. 6, pp. 2729–2742, 2015.

[25] S. Kokjohn, R. D. Reitz, D. Splitter, and M. Musculus, "Investigation of Fuel Reactivity Stratification for Controlling PCI Heat-Release Rates Using High-Speed Chemiluminescence Imaging and Fuel Tracer Fluorescence," *SAE Int. J. Engines*, vol. 5, no. 2, pp. 2012-01–0375, 2012.

[26] J. E. Dec and Y. Yang, "Boosted HCCI for High Power without Engine Knock and with Ultra-Low NOx Emissions - using Conventional Gasoline," *SAE Int. J. Engines*, vol. 3, no. 1, pp. 2010-01–1086, 2010.

[27] Y. B. Zeldovich, "Regime classification of an exothermic reaction with nonuniform initial conditions," *Combust. Flame*, vol. 39, no. 2, pp. 211–214, 1980.

[28] X. J. Gu, D. R. Emerson, and D. Bradley, "Modes of reaction front propagation from hot spots," vol. 133, pp. 63–74, 2003.

[29] A. E. Lutz, R. J. Kee, J. A. Miller, H. A. Dwyer, and A. K. Oppenheim, "Dynamic effects of autoignition centers for hydrogen and C1,2-hydrocarbon fuels," *Symp. Combust.*, vol. 22, no. 1, pp. 1683–1693, 1989.

[30] L. Bates, D. Bradley, G. Paczko, and N. Peters, "Engine hot spots : Modes of auto-ignition and reaction propagation," vol. 166, pp. 80–85, 2016.

[31] M. B. Luong, G. H. Yu, S. H. Chung, and C. S. Yoo, "Ignition of a lean PRF/air mixture under RCCI/SCCI conditions: A comparative DNS study," *Proc. Combust. Inst.*, vol. 36, no. 3, pp. 3623–3631, 2017.

[32] M. B. Luong, R. Sankaran, G. H. Yu, S. H. Chung, and C. S. Yoo, "On the effect of injection timing on the ignition of lean PRF/air/EGR mixtures under direct dual fuel stratification conditions," *Combust. Flame*, vol. 183, pp. 309–321, 2017.

[33] M. B. Luong, R. Sankaran, G. H. Yu, S. H. Chung, and C. S. Yoo, "A DNS study of the effects of injection timing on the ignition of lean PRF/air/EGR mixture with composition inhomogeneities relevant to RCCI/DDFS combustion," *Combust. Flame*, vol. 183, no. May, p. Submitted to CNF, 2017.

[34] J. Neuman, "Development of a Rapid Compression Controlled-Expansion Machine for Chemical Igntion Studies," Marquette University, 2015.

[35] G. Mittal, "A Rapid Compression Machine-Design, Characterization, and Autoigniton Investigations," Case Western R, 2006.

[36] C. Allen, G. Mittal, C. J. Sung, E. Toulson, and T. Lee, "An aerosol rapid compression machine for studying energetic-nanoparticle- enhanced combustion of liquid fuels," *Proc. Combust. Inst.*, vol. 33, no. 2, pp. 3367–3374, 2011.

[37] S. S. Goldsborough, S. Hochgreb, G. Vanhove, M. S. Wooldridge, H. J. Curran, and C. J. Sung, "Advances in rapid compression machine studies of low- and intermediate-temperature autoignition phenomena," *Prog. Energy Combust. Sci.*, vol. 63, pp. 1–78, 2017.

[38] R. Minetti, M. Carlier, M. Ribaucour, E. Therssen, and L. R. Sochet, "A rapid compression machine investigation of oxidation and auto-ignition of n-Heptane: Measurements and modeling," *Combust. Flame*, vol. 102, no. 3, pp. 298–309, 1995.

[39] G. Mittal and C. J. Sung, *A rapid compression machine for chemical kinetics studies at elevated pressures and temperatures*, vol. 179, no. 3. 2007.

[40] G. Kukkadapu, K. Kumar, C. J. Sung, M. Mehl, and W. J. Pitz, "Autoignition of gasoline surrogates at low temperature combustion conditions," *Combust. Flame*, vol. 162, no. 5, pp. 2272–2285, 2015.

[41] C.-J. Sung and H. J. Curran, "Using rapid compression machines for chemical kinetics studies," *Prog. Energy Combust. Sci.*, vol. 44, pp. 1–18, 2014.

[42] J. L.H.S.Roblee, "A Technique for Sampling Reaction Intermediates in a Rapid Compression Machine," *Combust. Flame*, vol. 5, no. 814, p. 7, 1960.

[43] X. He, S. M. Walton, B. T. Zigler, M. S. Wooldridge, and A. Atreya, "Experimental investigation of the intermediates of isooctane during ignition," *Int. J. Chem. Kinet.*, vol. 39, no. 9, pp. 498–517, Sep. 2007.

[44] G. Gentz, B. Thelen, P. Litke, J. Hoke, and E. Toulson, "Combustion Visualization, Performance, and CFD Modeling of a Pre-Chamber Turbulent Jet Ignition System in a Rapid Compression Machine," *SAE Int. J. Engines*, vol. 8, no. 2, pp. 2015-01–0779, 2015.

[45] H. Hu and J. Keck, "Autoignition of Adiabatically Compressed," *Fuels Lubr.*, vol. 96, no. 7, pp. 592–604, 1987.

[46] G. Mittal and C. J. Sung, "Aerodynamics inside a rapid compression machine," *Combust. Flame*, vol. 145, no. 1–2, pp. 160–180, 2006.

[47] Z. Wang, Y. Qi, X. He, J. Wang, S. Shuai, and C. K. Law, "Analysis of pre-ignition to super-knock: Hotspot-induced deflagration to detonation," *Fuel*, vol. 144, pp. 222–227, 2015.

[48] J. F. Griffiths, J. P. MacNamara, C. G. W. Sheppard, D. A. Turton, and B. J. Whitaker, "The relationship of knock during controlled autoignition to temperature inhomogeneities and fuel reactivity," *Fuel*, vol. 81, no. 17, pp. 2219–2225, 2002.

[49] M. Pöschl and T. Sattelmayer, "Influence of temperature inhomogeneities on knocking combustion," *Combust. Flame*, vol. 153, no. 4, pp. 562–573, 2008.

[50] T. Hayashi, M. Taki, S. Kojima, and T. Kondo, "Photographic Observation of Knock with a Rapid Compression and Expansion Machine," *SAE Tech. Pap. Ser.*, vol. 1, no. 1984, pp. 847–859, 2010.

[51] McMaster-Carr, "Ultra-High-Temperature Mineral Wool Insulation Tube 1" Thick Wall, 2-3/8" ID, 3 Feet Long." [Online]. Available: https://www.mcmaster.com/9364k16.

[52] Y. Cengel and R. Turner, "Mechanisms of Heat Transfer," in *Fundementals of Thermal-Fluid Sciences*, 1st ed., McGraw-Hill, 2005, pp. 714–715.

[53] "Midland Plastics: Polycarbonate." [Online]. Available: https://www.midlandplastics.com/materials-distribution/polycarbonate.

[54] J. T. Farrell *et al.*, "Development of an Experimental Database and Kinetic Models for Surrogate Diesel Fuels," vol. 2007, no. 724, pp. 776–790, 2007.

[55] T. Mun Foong, K. J. Morganti, M. J. Brear, Y. Yang, and F. L. Dryer, "The octane numbers of ethanol blended with gasoline and its surrogates," *Fuel*, vol. 115, pp. 727–739, 2014.

[56] D. Kim *et al.*, "A Study of Emissions Reduction through Dual-Fuel Combustion with Propane in a Compression Ignition Engine," *SAE Tech. Pap. Ser.*, vol. 1, 2013.

[57] J. Lee, S. Choi, H. Kim, D. Kim, H. Choi, and K. Min, "Reduction of Emissions with Propane Addition to a Diesel Engine," *Int. J. Automot. Technol.*, vol. 14, no. 4, pp. 551–558, 2013.

[58] K. A. Hodges, A. Aniello, S. R. Krishnan, and K. K. Srinivasan, "Impact of propane energy fraction on diesel-ignited propane dual fuel low temperature combustion," *Fuel*, vol. 209, no. April, pp. 769–775, 2017.

[59] K. J. Morganti, T. M. Foong, M. J. Brear, G. Da Silva, Y. Yang, and F. L. Dryer, "The research and motor octane numbers of Liquefied Petroleum Gas (LPG)," *Fuel*, vol. 108, pp. 797–811, 2013.

[60] A. D. Puckett, "Knock ratings of gasoline substitutes," *J. Res. Natl. Bur. Stand. (1934).*, vol. 35, no. 4, p. 273, 1945.

[61] C. Allen, E. Toulson, T. Edwards, and T. Lee, "Application of a novel charge preparation approach to testing the autoignition characteristics of JP-8 and camelina hydroprocessed renewable jet fuel in a rapid compression machine," *Combust. Flame*, vol. 159, no. 9, pp. 2780–2788, 2012.

[62] J. Pan, P. Zhao, C. K. Law, and H. Wei, *A predictive Livengood–Wu correlation for two-stage ignition*, vol. 17, no. 8. 2016.

[63] C. Allen, D. Valco, E. Toulson, T. Edwards, and T. Lee, "Ignition behavior and surrogate modeling of JP-8 and of camelina and tallow hydrotreated renewable jet fuels at low temperatures," *Combust. Flame*, vol. 160, no. 2, pp. 232–239, 2013.

[64]   A. B. Mansfield, M. S. Wooldridge, H. Di, and X. He, "Low-temperature ignition behavior of iso-octane," *Fuel*, vol. 139, pp. 79–86, 2015.

[65]   A. B. Mansfield and M. S. Wooldridge, "High-pressure low-temperature ignition behavior of syngas mixtures," *Combust. Flame*, vol. 161, no. 9, pp. 2242–2251, 2014.

[66]   S. Jensen, "No One Fuel Solution," *OEM Off-Highway*, 2019. [Online]. Available: https://www.oemoffhighway.com/engines/fuels-fluids/article/21046823/no-one-fuel-solution.

[67]   S. Collins, "Clash of Cultures," *Racecar Engineering*, Leicestershire, UK, pp. 8–16, Dec-2018.